Bowdoin College

# Bowdoin Digital Commons

2023

# Properties of Slicing Conditions for Charged Black Holes

Sean E. Li
*Bowdoin College*

# Properties of Slicing Conditions for Charged Black Holes

An Honors Paper for the Department of Physics and Astronomy

By Sean E. Li

Bowdoin College, 2023

# Abstract

We consider an earlier analysis by Baumgarte and de Oliveira (2022) of static Bona-Massó slices of stationary, nonrotating, uncharged black holes, represented by Schwarzschild spacetimes, and generalize that approach to Reissner-Nordström (RN) spacetimes, representing stationary, nonrotating black holes that carry a nonzero charge. This charge is parametrized by the charge-to-mass ratio $\lambda \equiv Q/M$, where $M$ is the black-hole mass and the charge $Q$ may represent electrical charge or act as a placeholder for extensions of general relativity. We use a height-function approach to construct time-independent, spherically symmetric slices that satisfy a so-called Bona-Massó slicing condition. We compute quantities such as critical points and profiles of geometric quantities for several different versions of the Bona-Massó slicing condition. In some cases we do this analytically, while in others we use numerical root-finding to solve quartic equations. We conclude that in the extremal limit as $\lambda \to 1$, all slices that we consider approach a unique slice that is independent of the chosen Bona-Massó condition.

We then study dynamical, i.e. time-dependent, Bona-Massó slices by analytically predicting the qualitative behavior of the central lapse, i.e. the lapse at the black-hole puncture, for a particular slice that Alcubierre (1997) proposed to mitigate gauge shocks. These shock-avoiding slices are a viable alternative to the very common so-called $1 + \log$ slices but exhibit different behavior in dynamical simulations. We use a perturbation of the radial coordinate at the location of the puncture to recover approximately harmonic late-time oscillations of the central lapse that Baumgarte and Hilditch (2022) observed in numerical simulations.

# Contents

# List of Figures

# 1 Introduction

## 1.1 General Relativity

General relativity (GR) is a relativistic theory of gravity [1] governed by a set of nonlinear, coupled partial differential equations (PDEs) known as Einstein's equations,

$$R_{ab} - \frac{1}{2} R g_{ab} + \Lambda g_{ab} = 8\pi T_{ab}. \tag{1.1}$$

Here $R_{ab}$ is the Ricci tensor, its trace $R \equiv R^a{}_a$ the Ricci scalar, $g_{ab}$ the spacetime metric, $\Lambda$ the cosmological constant, and $T_{ab}$ the stress-energy tensor.[1] (See Sec. 4.2 in [2] for the construction of these quantities). Einstein's equations relate the curvature of 4D spacetime, encoded by the Ricci tensor, to the density and flux of energy and momentum, encoded by the stress-energy tensor. The Ricci tensor can be computed from the spacetime metric $g_{ab}$, whose components act as coefficients in the invariant line element,

$$ds^2 = g_{ab} \, dx^a \, dx^b \,, \tag{1.2}$$

which measures distances between spacetime events. In GR, test objects follow their straightest possible paths—*geodesics*—through curved spacetimes absent external forces. For example, a satellite is not held in orbit by an attraction to Earth, but rather, unless

---

[1]In this thesis we use geometrized, or natural, units with $c = G = 1$ and $\varepsilon_0^{-1} = 4\pi$. In this system, length, mass, and charge all have units of time, or equivalently, time, mass, and charge all have units of length (and so on).

disturbed by a collision with space debris (e.g.) the satellite travels along a geodesic through spacetime curved by the mass of the Earth.

Einstein's equations admit gravitational waves as vacuum solutions, i.e. solutions in regions of spacetime where $T_{ab} = 0$. These are traveling perturbations of the metric that induce oscillatory contractions and expansions of spacetime itself. One hundred years after Einstein predicted [3] their existence, the Laser Interferometer Gravitational-Wave Observatory (LIGO) [4] detected gravitational radiation emitted by the coalescence of distant binary black holes. This discovery showed gravitational waves are viable astrophysical messengers that can transmit information about events that may be unavailable in the electromagnetic regime. Since the initial LIGO detection in 2015, gravitational-wave astronomy has rapidly advanced [5] and enabled empirical tests of GR in strong gravity [6]. Gravitational waves may yet provide insight into supermassive black holes at galactic centers, mergers of massive binaries, the evolution of black holes over cosmic time, and outstanding questions in gravitation, particle physics, and cosmology, such as quantum gravity and the nature of dark matter and energy [7–9].

To identify their astrophysical origins, gravitational-wave signatures are compared against the predictions of GR. However, the full Einstein equations are analytically intractable for many realistic astrophysical scenarios, such as the inspiral, merger, and ringdown of binary black holes, which produced the 2015 LIGO signal [4]. Therefore, for such scenarios, the equations of GR must be solved using numerical integration rather than hand calculations. This is not so straightforward, however.

## 1.2 Numerical Relativity

Numerical relativists use computers to integrate Einstein's equations of GR. Computers make predictions in full GR possible in principle, but numerical simulations employ discrete methods and are liable to crash where components of the spacetime metric diverge,

namely at the event horizon(s) and curvature singularity of a black-hole spacetime and possible coordinate singularities that may arise throughout the simulation. To avoid these numerical pitfalls, researchers routinely exploit so-called *gauge freedom* to transform to more suitable—and stable—coordinate systems. Einstein's equations and their physical solutions are invariant under these coordinate transformations, so one may represent the same physical problem in various ways.

## 3 + 1 Formalism

The standard approach to numerically integrating Einstein's equations involves a so-called 3+1 decomposition that separates time derivatives and components from their spatial counterparts. Arnowitt, Deser, and Misner (ADM) introduced this formalism in 1962 [10] and Smarr and York [11] made refinements in 1978. The $3 + 1$ approach breaks Einstein's equations into constraint equations that the initial data must satisfy and evolution equations that govern the time evolution. The evolution equations are made to be consistent with the constraint equations, assuring that the data will satisfy the constraints for all time, provided they satisfy the constraints initially. Analogously with electromagnetism, wherein the $\mathbf{E}$ and $\mathbf{B}$ fields are invariant under a transformation of the vector potential $\mathbf{A} \rightarrow \mathbf{A} + \boldsymbol{\nabla}\phi$, where $\phi$ is an arbitrary gauge scalar, the 3+1 decomposition of Einstein's equations introduces free gauge[2] variables that do not affect the physics but play a vital role in designing an apt numerical simulation (see Sec. 2.3 in [12] for a concise pedagogical overview).

The original ADM formalism was an essential prerequisite for working with full general relativity on the computer and was widely adopted. Shibata and Nakamura (1995) [13] and Baumgarte and Shapiro (1998) [14] modified the standard ADM equations to achieve great improvements in stability for simulating gravitational waves over long time

---

[2]Coordinate conditions play the same role in general relativity as gauge conditions in electromagnetism. Unless otherwise noted, in this thesis we will use the terms "gauge" and "coordinate" interchangeably hereafter.
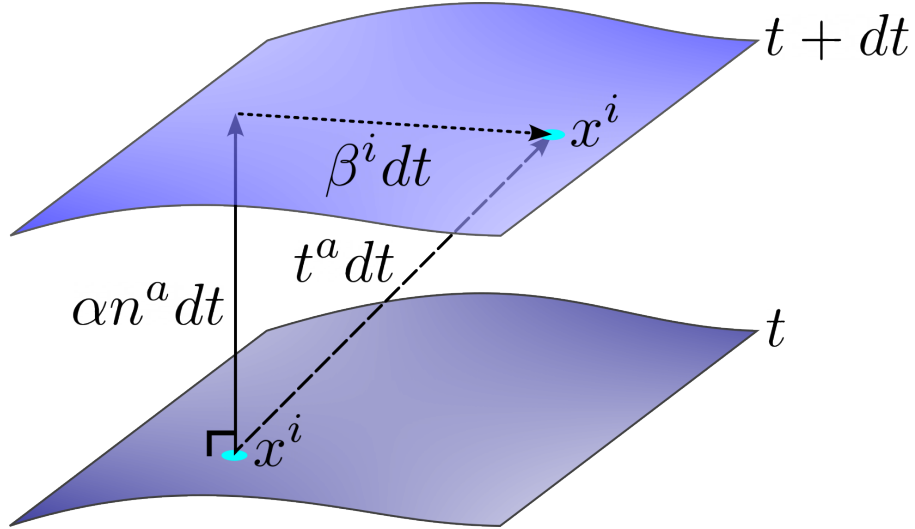
Figure 1.1: An illustration of the normal $n^a$ and lapse $\alpha$ (solid line) and shift $\beta^i$ (dotted line) between spatial hypersurfaces at coordinate times $t$ and $t + dt$. The vector $t^a = \alpha n^a + b^a$ (dashed line) connects points with the same spatial coordinate $x^i$ between hypersurfaces.

scales. The so-called Baumgarte-Shapiro-Shibata-Nakamura (BSSN) formalism has since been adopted by many authors as a default (see, e.g., [15–19]).

Conditions on the time coordinate may be interpreted geometrically as generating the shape of so-called *slices* of spacetime. These are spatial hypersurfaces constant in a chosen time coordinate $t$ that are separated by intervals $dt$. The 4D spacetime is thus *foliated* by slices of three spatial dimensions stacked along a temporal axis. In order to visualize these slices in two dimensions, we need to remove one degree of freedom; e.g., by taking a cross section in the equatorial plane with $\theta = \pi/2$. The curvature of the slices is apparent when the slices are *embedded* in a diagram of one dimension higher (see Fig. 1.1). In this thesis we will work with several important geometric quantities that describe the spatial hypersurfaces; these are introduced below.[3]

## Spacetime Geometry

Whereas $t$ denotes coordinate time, the proper time $\tau$ is the time that an observer measures. The normal vector $n^a$ is orthogonal to the spatial slices; here we choose the

---

[3]The following discussion of the geometry of spacetime slices is derived from [20].

4

normal to be future-oriented, that is, pointing in the direction of increasing coordinate time. The lapse function $\alpha \equiv d\tau/dt$ measures the advance of time between adjacent spatial slices. More precisely, the lapse is the ratio of the elapsed proper time $d\tau$ for an observer following the normal (a *normal observer*) between slices to the change in coordinate time $dt$ between slices. An observer whose spatial coordinates $x^i$ are held constant is said to be a *coordinate observer*. The shift vector $\beta^i$ measures the coordinate displacement $\Delta x^i$ of a coordinate observer relative to a normal observer between adjacent slices. The normal, lapse, and shift are illustrated in Fig. 1.1.

The spatial metric $\gamma_{ab} = g_{ab} + n_a n_b$ is the purely spatial projection of the spacetime metric $g_{ab}$ onto the hypersurface and measures spatial distances (i.e. with no component normal to the surface). Since $\gamma_{0a} = 0$ we hereafter write the spatial metric with spatial indices $ij$ as opposed to spacetime indices $ab$. From the spatial metric we can define the extrinsic curvature $K_{ab} \equiv -\gamma_a{}^c \gamma_b{}^d \nabla_c n_d$ whose trace $K \equiv K^i{}_i$ we refer to as the *mean curvature*. In words, the extrinsic curvature is the spatial projection of the covariant derivative $\nabla$ of the normal along the hypersurface. Since $K_{ab}$ is a spatial tensor by construction, we will restrict its indices to spatial indices.

## Coordinate Conditions

In terms of the $3+1$ quantities introduced above, the line element (1.2) can now be expressed as

$$ds^2 = \alpha^2 \, dt^2 + \gamma_{ij} \big(dx^i + \beta^i \, dt\big)\big(dx^j + \beta^j \, dt\big). \tag{1.3}$$

We now use $\bar{t}$ to denote the time coordinate in the original spacetime metric and let $t$ denote a new time coordinate. We may then transform $\bar{t}$ to $t$ using a so-called *height-function* approach. As Fig. 1.2 illustrates, the height function $h$ measures the distance between the new slices of constant $t$ and the old slices of constant $\bar{t}$. For static slices in spherical
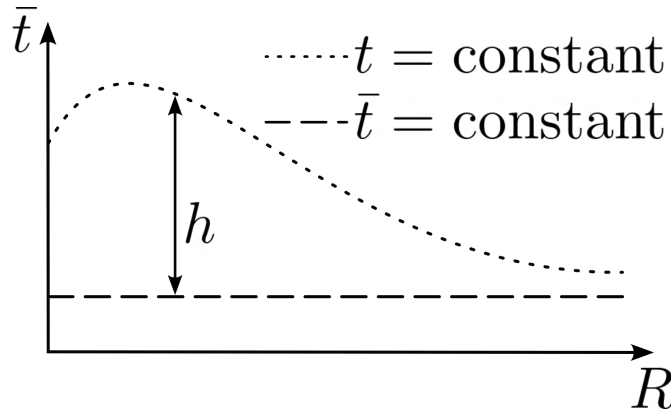
Figure 1.2: Slices of constant coordinate times $t$ and $\bar{t}$ related by a height function.

symmetry, $h = h(R)$, while for dynamical slices in spherical symmetry, $h = h(t, R)$. By substituting the new time coordinate into a given spacetime metric and comparing with the $3 + 1$ line element (1.3), one may identify the lapse, spatial metric, and shift on the slices in terms of the height function. We will detail this approach in Ch. 3.

Early *singularity-avoiding* gauge conditions such as maximal slicing ($K = \partial_t K = 0$) constructed slices that ended before the black-hole singularity, but these were prone to so-called grid stretching that made the spacetime near the singularity hard to resolve over long time scales [21]. In 2005, the *annus mirabilis* of numerical relativity, three seminal papers [22–24] made breakthroughs in dynamical black-hole binary simulations. Pretorius [22, 25] introduced so-called generalized harmonic coordinates implemented via gauge source functions and demonstrated that this scheme was stable enough to produce data from the inspiral, merger, and gravitational-wave emissions of a binary black-hole spacetime. Also that year, Campanelli et al. [23] and Baker et al. [24] used the BSSN formalism and an algebraic gauge condition introduced by Bona and Massó et al. [26] in 1995, known as *Bona-Massó slicing*, to achieve remarkably successful simulations. The so-called *moving puncture* gauge improved on the *puncture method* introduced by Brügmann in 1999 [21], which avoided the physical singularity in favor of a static (time-independent) coordinate singularity known as the puncture. The puncture could now move across the grid, and stable, long-term evolutions became possible. However, why this approach
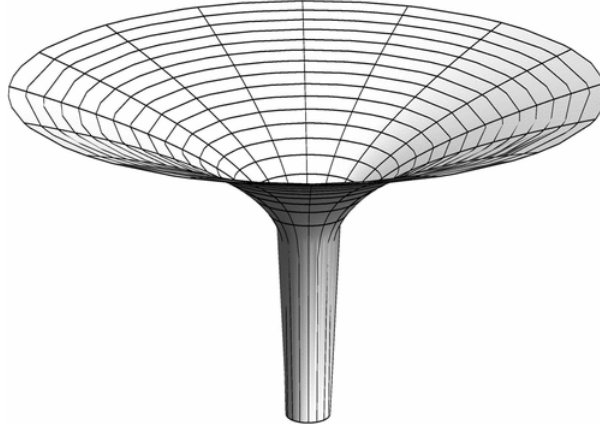
Figure 1.3: Figure 2 in Hannam et al. (2008) [28] shows an embedding diagram of a trumpet slice of the Schwarzschild spacetime. The asymptotically cylindrical end represents the black-hole puncture, while the asymptotically flat end represents spatial infinity.

worked so well was unclear; in particular, what happens to the puncture as the spacetime is evolved and whether the evolution terminates in a stationary slice was a mystery (see [27] for an overview of the status of numerical relativity at the time).

The desire to understand these breakthroughs motivated researchers to return to a much simpler, analytically known spacetime, namely the Schwarzschild spacetime, representing a single stationary black hole in spherical symmetry and the simplest exact solution to Einstein's equations. Hannam et al. (2007) [16] examined the geometry of stationary Bona-Massó slices of Schwarzschild spacetimes, revealing that the puncture in such slices converges to an infinitely long, asymptotically cylindrical "throat" with a finite areal radius[4] $R$, thereby avoiding the physical singularity without inducing grid stretching. In the limit as $R \to \infty$, the slice is asymptotically flat, i.e. the spacetime metric approaches the Minkowski metric. These slices are called *trumpet slices* due to their geometry, which the embedding diagram in Fig. 1.3 illustrates.

---

[4]The areal radius is computed as the ratio of the proper circumference of the cylinder to $2\pi$.

## 1.3　The Black-Hole Charge

While the Schwarzschild spacetime is commonly used as a simple test case for coordinate conditions in numerical relativity, a number of authors [29–40] have recently considered the astrophysical role of the black-hole charge and simulated the interactions of charged black holes, whose spacetimes are given by the Reissner-Nordström (RN) metric. Bozzola and Paschalidis [36], for example, showed that an upper bound on the black-hole charge can be recovered from gravitational-wave data and also used the charge parameter to quantify empirical deviation from general relativity in the context of modified theories of gravity. The electrical charge of black holes is often assumed negligible due to the low likelihood of accreting an appreciable net charge and neutralization due to vacuum polarization [41]. Though the charge $Q$ can represent electrical charge, it can also represent magnetic charge (supposing that magnetic monopoles exist) or so-called *dark charge* associated with $U(1)$ symmetry (see [35]), or act as a placeholder term for modified theories of gravity such as the scalar-tensor-vector theory proposed by Moffat [42].

# 2   Solutions to Einstein's Equations

## 2.1   The Schwarzschild Spacetime

Representing a single static black hole in spherical symmetry, the Schwarzschild spacetime [43] is the simplest exact solution to the Einstein equations. The line element expressed in Schwarzschild coordinates is

$$ds^2 = -\left(1 - \frac{2M}{R}\right) dt^2 + \left(1 - \frac{2M}{R}\right)^{-1} dR^2 + R^2\, d\Omega^2\,, \tag{2.1}$$

where $M$ is the mass of the black hole and $R$ the areal radius, and the differential solid angle $d\Omega = \sin\theta\, d\theta\, d\phi$. Evidently, the metric component

$$g_{tt} = -\left(1 - \frac{2M}{R}\right) \tag{2.2}$$

diverges at $R = 0$. This location marks the physical *singularity* at the center of the black hole. Observe also that the component

$$g_{RR} = \left(1 - \frac{2M}{R}\right)^{-1} \tag{2.3}$$

diverges at $R = 2M$. This is the *event horizon*, which marks the boundary of the black-hole interior. Within the radius of the event horizon, all worldlines (trajectories through spacetime) point toward the singularity; therefore, once the event horizon is crossed, not

even null paths (i.e. light) can re-emerge from the black hole. Since no light, and hence no information, can travel from within the black-hole interior to the surrounding spacetime, events whose radial coordinate $R < 2M$ cannot causally affect events on the outside.

According to the so-called *no-hair theorem* [44–46], all black holes are fully characterized by just three parameters: their mass, charge, and spin. Representing a black hole whose charge and spin are zero, the Schwarzschild spacetime has been used for its analytical amiability to understand coordinate conditions used to simulate black-hole binaries. However, the Schwarzschild spacetime can be generalized easily to black holes with nonzero charge by the addition of a charge term in the metric components (2.2) and (2.3). Such black holes are represented by the Reissner-Nordström spacetime [47].

## 2.2 The Reissner-Nordström Spacetime

Expressed in Schwarzschild coordinates, the Reissner-Nordström line element is

$$ds^2 = -\left(1 - \frac{2M}{R} + \frac{Q^2}{R^2}\right) dt^2 + \left(1 - \frac{2M}{R} + \frac{Q^2}{R^2}\right)^{-1} dR^2 + R^2 \, d\Omega^2 \,, \qquad (2.4)$$

where $Q$ is the black-hole charge. Since the charge-to-mass ratio $\lambda \equiv Q/M$ is expected to be small in most astrophysical scenarios, this term is often ignored (see Sec. 1.3), reducing the metric to Schwarzschild. In this thesis we are motivated to work with the RN metric by recent studies of charged black-hole binaries and assessments of the role of the black-hole charge [29–40]. Moreover, the charge is of theoretical interest due to the possibility of so-called *naked singularities*, i.e. singularities that are not concealed by an event horizon, which *super-extremal* RN spacetimes with $\lambda > 1$ would possess. To see this, we again locate the horizon at a root of the function

$$g_{tt} = -\left(1 - \frac{2M}{R} + \frac{Q^2}{R^2}\right), \qquad (2.5)$$

given by

$$R = M \pm \sqrt{M^2 - Q^2} \quad (Q > 0). \tag{2.6}$$

These two roots correspond to two event horizons, one inner ("−") and one outer ("+"). Evidently, in the extremal case $\lambda = 1 \implies Q = M$, these horizons converge at $R = M$. For $\lambda > 1 \implies Q > M$, the roots are imaginary and therefore no horizon exists. The metric components $g_{tt}$ and $g_{RR}$ still clearly diverge at $R = 0$, however, corresponding to a naked singularity. See Secs. 6.4 and 6.5 in [2] for a textbook discussion of the black-hole mass, spin, and charge and the RN spacetime, including naked singularities.

# 3 The Height-Function Approach

## 3.1 General Procedure

In this thesis we make transformations of the time coordinate using a *height function* that measures the distance between new and old time slices. In spherical symmetry we relate the new and old coordinate times—$t$ and $\bar{t}$, respectively—by

$$\bar{t} = t - h(t, R) \implies d\bar{t} = \left(1 - \dot{h}\right) dt - h' \, dR, \tag{3.1}$$

where the dot denotes a partial derivative with respect to time and a prime with respect to areal radius (i.e. $\dot{h} \equiv \partial h / \partial t$ and $h' \equiv \partial h / \partial R$). For static slices, $h = h(R)$ only. Consider a spacetime metric expressed in coordinate time $\bar{t}$ as

$$ds^2 = -F \, d\bar{t}^2 + F^{-1} \, dR^2 + R^2 \, d\Omega^2, \tag{3.2}$$

where $F = F(R)$ is an as yet unspecified function of the areal radius. Note that the real roots of $F$ correspond to the locations of the black-hole event horizons. We substitute the transformation (3.1) into the metric to obtain

$$ds^2 = -F\left(\left(1 - \dot{h}\right)^2 dt^2 - 2\left(1 - \dot{h}\right)h' \, dt \, dR + (h')^2 \, dR^2\right) + F^{-1} \, dR^2 + R^2 \, d\Omega^2$$
$$= -F\left(1 - \dot{h}\right)^2 dt^2 + 2F\left(1 - \dot{h}\right)h' \, dt \, dR - F^{-1}\left(1 - F^2(h')^2\right) dR^2 + R^2 \, d\Omega^2. \tag{3.3}$$

We now compare Eq. (3.3) with the general $3 + 1$ representation (1.3) of the spacetime metric. From this, we identify the $RR$-component of the spatial metric as

$$\gamma_{RR} = \frac{1 - F^2(h')^2}{F},$$

(3.4)

allowing us to identify the (contravariant) $R$-component of the shift via

$$\beta_R = \gamma_{RR}\beta^R = F\left(1 - \dot{h}\right)h'\, dt\, dR.$$

(3.5)

Dividing both sides of the second equality by $\gamma_{RR}$, we obtain

$$\beta^R = \frac{F^2\left(1 - \dot{h}\right)h'}{1 - F^2(h')^2}.$$

(3.6)

We observe in Eq. (3.3) that the angular components of the shift vanish, as expected in spherical symmetry.[1] Now we can compute the square of the lapse from

$$-\alpha^2 + \gamma_{RR}\left(\beta^R\right)^2 = -F\left(1 - \dot{h}\right)^2;$$

(3.7)

isolating the lapse, we obtain

$$\alpha^2 = F\left(1 - \dot{h}\right)^2 + \frac{F^3\left(1 - \dot{h}\right)^2(h')^2}{1 - F^2(h')^2} = \frac{F\left(1 - \dot{h}\right)^2}{1 - F^2(h')^2}.$$

(3.8)

Note that $\alpha$ and $\beta^R$ do not necessarily vanish at the horizon(s), where $F = 0$, since $h'$ may diverge there such that these quantities remain finite. Indeed, we later rely on this behavior to construct slices that penetrate the outer horizon, i.e. slices that connect a root of the lapse within the outer horizon to $\alpha \to 1$ in the asymptotic limit $R \to \infty$. To

---

[1]Since the shift vector $\beta^i = \left(\beta^R, 0, 0\right)$ in spherical symmetry, hereafter we refer to $\beta^R$ as simply "the shift" to reduce verboseness.

13

compute the mean curvature $K$, we invoke the identity[2]

$$\nabla_a A^a = \frac{1}{\sqrt{|g|}} \partial_a \left( \sqrt{|g|} A^a \right), \tag{3.9}$$

where the determinant $g$ of the spacetime metric can be written as

$$g = -\alpha^2 \gamma_{RR} R^4 \sin^2 \theta. \tag{3.10}$$

The mean curvature is then

$$K = -\nabla_a n^a = -\frac{1}{\sqrt{|g|}} \partial_a \left( \sqrt{|g|} n^a \right). \tag{3.11}$$

## 3.2   Static Slices

For static slices, i.e. $\dot{h} = 0$, the lapse (3.8) and the shift (3.6) reduce to

$$\alpha^2 = \frac{F}{1 - F^2 (h')^2} \tag{3.12a}$$

and

$$\beta^R = \frac{F^2 h'}{1 - F^2 (h')^2}, \tag{3.12b}$$

and we observe that the relations

$$\beta^R = \alpha \sqrt{\alpha^2 - F} \tag{3.13a}$$

---

[2]See, e.g., Solution 7.7 in Lightman et al. [48] for a derivation.

14

and

$$\gamma_{RR} = \alpha^{-2} \tag{3.13b}$$

allow us to eliminate the height function. (These do not hold for dynamical slices due to the presence of time derivatives of the height function, which cannot be eliminated.) By Eq. (3.11) and relation (3.13b), the static mean curvature becomes

$$K = \frac{1}{R^2} \frac{d}{dR} \left( R^2 \frac{\beta^R}{\alpha} \right) = \frac{2}{R} \frac{\beta^R}{\alpha} + \frac{\left(\beta^R\right)'}{\alpha} - \frac{\beta^R}{\alpha^2} \alpha'. \tag{3.14}$$

## The Black-Hole Puncture

We denote the areal coordinate where the lapse vanishes as $R_0$, i.e. $\alpha(R_0) = 0$, and the derivative of the lapse evaluated at its root as

$$a_1 \equiv \alpha'(R_0). \tag{3.15}$$

The root of the lapse terminates the slice. To leading order, relation (3.13b) implies that

$$\gamma_{RR} \simeq a_1^{-2}(R - R_0)^{-2} \quad (R \to R_0) \tag{3.16}$$

in the neighborhood of the root of the lapse. Assuming $0 < a_1 < \infty$, we can integrate the line element in this limit as

$$\int_{R_0}^{R} ds = \int_{R_0}^{R} \sqrt{\gamma_{RR}} \, d\tilde{R} = \int_{R_0}^{R} d\tilde{R} \, a_1^{-1} \left( \tilde{R} - R_0 \right)^{-1} = a_1^{-1} \ln \left( \tilde{R} - R_0 \right) \Big|_{R_0}^{R} = \infty. \tag{3.17}$$

We see that the root $R_0$ is located an infinite proper distance away from all points $R > R_0$, and therefore we refer to this location as the *black-hole puncture*. Expanding the lapse to leading order and rearranging Eq. (3.12a), we also observe also that, in the vicinity of the

puncture, the height function diverges according to

$$h_0' \simeq -\frac{1}{\sqrt{-F(R_0)}a_1(R - R_0)} \quad (R \to R_0), \qquad (3.18)$$

where we have adopted a negative sign in taking a square root.[3]

For static slices, the root of the lapse occurs where $h_0'$ diverges. As relation (3.13b) makes apparent, $\alpha \to 0$ implies $\gamma_{RR} \to \infty$ in the static case. We also note that, for static horizon-penetrating slices, for which the lapse is nonzero and finite on the outer horizon, Eq. (3.12a) indicates that the height function must diverge at the outer horizon, too, since $F = 0$ there. This latter divergence could have been avoided by starting with a horizon-penetrating coordinate system in Eq. (3.2), rather than with Schwarzschild or RN coordinates.

We have not yet chosen a coordinate gauge, so the analysis in this chapter is valid in general. In the next chapter we will proceed to implement various such gauge conditions and study the properties of the resulting slices.

---

[3]Note that $F(R_0) < 0$ since the root lies within the outer horizon, i.e. $R_0 < 2M$.

# 4   Static Bona-Massó Slices

This chapter discusses the collaborative work of Li, Baumgarte, Dennison and de Oliveira (2022) [49] with some additional detail.

## 4.1   Motivation

The Bona-Massó slicing condition was used to remarkable success in the 2005 numerical relativity breakthrough papers (see Sec. 1.2) and continues to be adopted in numerical simulations. The Bona-Massó equation is a PDE

$$\left(\partial_t - \beta^i \partial_i\right)\alpha = -\alpha^2 f(\alpha)K, \tag{4.1}$$

where $\alpha$ is the lapse, $\beta^i$ the shift vector, $K$ the mean curvature, and the *Bona-Massó function* $f(\alpha)$ a yet-to-be-chosen function of the lapse. Choices of $f(\alpha)$ generate particular Bona-Massó slices. One very common choice is $f(\alpha) = 2/\alpha$, for which, in the absence of a shift, one can show that the lapse becomes

$$\alpha = 1 + \ln\gamma, \tag{4.2}$$

where $\gamma$ is the determinant of the spatial metric, earning it the name "$1 + \log$" slicing (see [50]). In this thesis we will refer to the generalized form $f(\alpha) = k/\alpha$ as $1 + \log$ slicing, even though Eq. (4.2) follows from $k = 2$ only.

Studying $1 + \log$ slices of Schwarzschild spacetimes yielded insights into their advantages for numerical simulations of much more complicated spacetimes [16, 18, 28, 51]. Recently, Baumgarte and de Oliveira [52] explored the properties of static $1 + \log$ slices and static slices generated by some alternative choices of $f(\alpha)$ for Schwarzschild spacetimes. We are interested in whether these families of static slicing conditions retain their advantages with the introduction of a nonzero black-hole charge, i.e. whether they exhibit similar properties for RN spacetimes, the charged counterparts to Schwarzschild spacetimes. We therefore generalize the analysis in [52] to RN spacetimes, considering the following Bona-Massó functions $f(\alpha)$.

Following [52] we begin with $1 + \log$ slices, whose Bona-Massó function is

$$f(\alpha) = \frac{k}{\alpha}, \tag{4.3}$$

since this choice (with $k = 2$) is very common and has proven remarkably successful. Dennison and Baumgarte (2014) [53] proposed the alternative

$$f(\alpha) = \frac{1 - \alpha}{\alpha} \tag{4.4}$$

for constructing trumpet slices that can be understood entirely analytically, making them valuable test cases, and as in [52] we consider this choice also. The remaining two Bona-Massó functions we consider were designed by Alcubierre [54, 55] to mitigate so-called gauge shocks. These are coordinate discontinuities that arise during the evolution of the spacetime and can propagate across the grid faster than light. Fully *shock-avoiding slices* are given by

$$f(\alpha) = 1 + \frac{\kappa}{\alpha^2} \tag{4.5}$$

where we require that the constant $\kappa > 0$. Despite their advantages in numerical

18

simulations (see, e.g., [56, 57]), these slices allow the lapse to become negative over the course of a numerical evolution [54, 55, 57]. Therefore we follow [52] in also considering slices that avoid gauge shocks to leading order only and whose lapse is not liable to become negative. The corresponding Bona-Massó function is

$$f(\alpha) = \frac{a_0^2}{2\alpha + (a_0 - 2)\alpha^2} \tag{4.6}$$

and these slices are called *zero order shock-avoiding slices* [55].

## 4.2   Methods

### Coordinate Transformation

The Reissner-Nordström metric is given by Eq. (3.2) with

$$F(R) = 1 - \frac{2M}{R} + \frac{Q^2}{R^2}. \tag{4.7}$$

For static and spherically symmetric slices, the Bona-Massó equation (4.1) reduces to

$$\beta^R \alpha' = \alpha^2 f(\alpha) K. \tag{4.8}$$

Substituting our result for the static mean curvature (3.14) into Eq. (4.8), we have

$$\beta^R \alpha' = \alpha^2 f(\alpha) \left( \frac{2}{R} \frac{\beta^R}{\alpha} + \frac{\left(\beta^R\right)'}{\alpha} - \frac{\beta^R}{\alpha^2} \alpha' \right). \tag{4.9}$$

We can separate variables to rewrite this as

$$\frac{d\alpha}{\alpha f(\alpha)} + \frac{d\alpha}{\alpha} = 2\frac{dR}{R} + \frac{d\beta^R}{\beta^R} \tag{4.10}$$

19

and integrate to obtain the equation

$$\int_0^\alpha \frac{d\tilde\alpha}{\tilde\alpha f(\tilde\alpha)} + C_0 + \ln\alpha = 2\ln R + \ln\beta^R \tag{4.11}$$

where $C_0$ is a constant of integration. Collecting the logarithms, we have

$$\ln\left(R^2\frac{\beta^R}{\alpha}\right) = C_0 + \int_0^\alpha \frac{d\tilde\alpha}{\tilde\alpha f(\tilde\alpha)}. \tag{4.12}$$

Writing $C_0 \equiv (1/2)\ln C$ where the new constant $C$ has units of $M^4$ and applying the relation (3.13a), we obtain the equation

$$R^2\sqrt{\alpha^2 - F} = \sqrt{C}\,e^{I(\alpha)}, \tag{4.13}$$

where $I(\alpha)$ is defined as the integral

$$I(\alpha) \equiv \int_0^\alpha \frac{d\tilde\alpha}{\tilde\alpha f(\tilde\alpha)}. \tag{4.14}$$

Isolating the lapse, we arrive at the result

$$\alpha^2 = 1 - \frac{2M}{R} + \frac{Q^2}{R^2} + \frac{C e^{2I(\alpha)}}{R^4}. \tag{4.15}$$

This equation for the lapse is identical to Eq. (13) in [52] for Schwarzschild slices except for the appearance of the charge term.

## Regularity Condition

The constant of integration in Eq. (4.15) is as yet undetermined. However, following [27, 28] we can choose $C$ by imposing a regularity condition for the derivative of the lapse.

Consider Eq. (4.8). Using relation (3.13a), the mean curvature (3.14) becomes

$$K = \frac{2}{R}\sqrt{\alpha^2 - F} + \frac{1}{\alpha}\left(\alpha'\sqrt{\alpha^2 - F} + \frac{\alpha(2\alpha\alpha' - F')}{2\sqrt{\alpha^2 - F}}\right) - \frac{\alpha'\sqrt{\alpha^2 - F}}{\alpha}$$
$$= \frac{2}{R}\sqrt{\alpha^2 - F} + \frac{2\alpha\alpha' - F'}{2\sqrt{\alpha^2 - F}}. \tag{4.16}$$

Now if we apply relation (3.13a) to Eq. (4.8) prior to integrating, we obtain

$$\alpha\sqrt{\alpha^2 - F}\,\alpha' = \alpha^2 f(\alpha)\left(\frac{2}{R}\sqrt{\alpha^2 - F} + \frac{2\alpha\alpha' - F'}{2\sqrt{\alpha^2 - F}}\right). \tag{4.17}$$

Multiplying both sides by the term $\sqrt{\alpha^2 - F}$, this becomes

$$R(\alpha^2 - F)\alpha' = 4\alpha f(\alpha)(\alpha^2 - F) + 2R\alpha^2 f(\alpha)\alpha' - R\alpha f(\alpha)F'. \tag{4.18}$$

Now collecting the $\alpha'$ terms we have

$$2R(\alpha^2 - F - \alpha^2 f(\alpha))\alpha' = \alpha f(\alpha)(4\alpha^2 - 4F - RF'). \tag{4.19}$$

Solving for $\alpha'$ yields

$$\alpha' = \frac{\alpha f(\alpha)}{2R}\frac{4\alpha^2 - 4F - RF'}{\alpha^2(1 - f(\alpha)) - F}, \tag{4.20}$$

thus isolating the radial derivative of the lapse. Now inserting Eq. (4.7) with

$$F'(R) = \frac{2M}{R^2} - \frac{2Q^2}{R^3}, \tag{4.21}$$

our equation (4.20) for the derivative of the lapse becomes

$$\alpha' = \frac{\alpha f(\alpha)}{2R} \frac{4\alpha^2 - 4 + 8M/R - 4Q^2/R^2 - 2M/R + 2Q^2/R^2}{\alpha^2(1 - f(\alpha)) - 1 + 2M/R - Q^2/R^2}$$

$$= \frac{\alpha f(\alpha)}{R} \frac{2 - 3M/R + Q^2/R^2 - 2\alpha^2}{1 - 2M/R + Q^2/R^2 + \alpha^2(f(\alpha) - 1)}. \tag{4.22}$$

We now observe that the denominator of the right-hand side of Eq. (4.22) may vanish at a radius beyond the root $R_0$ of the lapse, causing $\alpha'$ to diverge. We are interested in trumpet slices whose lapse is continuous in the region $R \in [R_0, \infty)$ and penetrates the outer horizon[1] $R_+$ such that $\alpha$ vanishes at $R_0 \in (R_-, R_+)$ (see [58]). Assuming the term $\alpha^2(f(\alpha) - 1) = 0$ for $\alpha = 0$ and that $f(\alpha) > 1$ for all $\alpha$, horizon-penetrating slices necessarily go through a critical point between the root of the lapse and the outer horizon.[2] This is because $F(R_+) = 0$ and $-\alpha(R_0)^2(f(\alpha(R_0)) - 1) = 0$; both these functions are non-positive in the region $R \in [R_0, R_+]$ and intersect so that the denominator of the right-hand side of Eq. (4.22) vanishes. Therefore we must avoid the consequent irregularity in $\alpha$ by requiring that the numerator of the right-hand side of Eq. (4.22) vanish at the same location as the denominator, keeping $\alpha'$ finite. To determine such a *critical point* $(\alpha_c, R_c)$, where $\alpha_c$ is the *critical lapse* and $R_c$ the *critical radius*, we consider the system of equations

$$2 - \frac{3M}{R_c} + \frac{Q^2}{R_c^2} - 2\alpha_c^2 = 0 \tag{4.23a}$$

and

$$1 - \frac{2M}{R_c} + \frac{Q^2}{R_c^2} + \alpha_c^2 f(\alpha_c) - \alpha_c^2 = 0. \tag{4.23b}$$

---

[1]Slices that penetrated the inner horizon also would have an imaginary lapse at the horizons by the following argument. If $R_0 < R_-$ then $F(R_0) > 0$, meaning we could evaluate Eq. (4.15) at the root $R_0$ to conclude $C < 0$. At the radii $R_-$ and $R_+$ of the horizons, where $F$ vanishes, we would then have $\alpha^2 < 0$, whose solutions are imaginary.

[2]The assumption $f(\alpha) > 1$ for all $\alpha$ is true for all slices we consider except the analytical trumpets given by Eq. (4.4), which may be constructed so as to avoid a critical point altogether.

We can eliminate the charge by subtracting Eq. (4.23b) from Eq. (4.23a) to obtain

$$1 - \frac{M}{R_c} - \alpha_c^2(f(\alpha_c) + 1) = 0. \tag{4.24}$$

Solving for the critical radius, we have

$$R_c = \frac{M}{1 - \alpha_c^2(f(\alpha_c) + 1)}. \tag{4.25}$$

Substituting this expression for the critical radius back into Eq. (4.23a), we have

$$0 = 2 - 3\big(1 - \alpha_c^2(f(\alpha_c) + 1)\big) + \frac{Q^2}{M^2}\big(1 - \alpha_c^2(f(\alpha_c) + 1)\big)^2 - 2\alpha_c^2$$

$$= \lambda^2(f(\alpha_c) + 1)^2\alpha_c^4 + \big((f(\alpha_c) + 1)(3 - 2\lambda^2) - 2\big)\alpha_c^2 + \lambda^2 - 1. \tag{4.26}$$

For some choices of $f(\alpha)$, this quartic equation for the critical lapse simplifies considerably and we can obtain $\alpha_c$ analytically. For others we use numerical root-finding for various specific values of $\lambda$. Given $\alpha_c$ we can recover $R_c$ from Eq. (4.25), and then, if the integral $I(\alpha)$ (4.14) is known analytically, substitute both these results into Eq. (4.15) to compute the constant of integration $C$ that ensures the regularity of the lapse.

Note that the above procedure works only if $\alpha f(\alpha)$ remains finite in the limit $\alpha \to 0$. This condition holds for all slices we consider here except for the shock-avoiding slices given by Eq. (4.5). For those slices,

$$\alpha f(\alpha) = \frac{\alpha^2 + \kappa}{\alpha}, \tag{4.27}$$

which diverges when $\alpha$ vanishes. The denominator of the right-hand side of Eq. (4.22) therefore vanishes at $\alpha = 0$, meaning that (provided the parameter $\kappa$ obeys a certain condition that we later discuss) the critical radius coincides with the root of the lapse rather than the solution to Eq. (4.23b).

23

## The Root of the Lapse

For these static slices, we identify the black-hole puncture as the location where the lapse vanishes. Having chosen $C$, we can compute the root $R_0$ of the lapse by evaluating Eq. (4.15) at $\alpha = 0$. As with the critical lapse and radius, for some slices we can do this analytically, while for others we use numerical root-finding. Next, we follow [52] in studying the behavior of the lapse profile in the vicinity of the puncture. To do this we compute the derivative $a_1$ of the lapse evaluated at its root, in most cases via implicit differentiation of Eq. (4.15), except for the shock-avoiding condition (4.5), for which it is more convenient to take the limit $R \to R_0$ of Eq. (4.22). In order to choose valid roots $R_0$ among the real solutions to the quartic equation (4.15), we check that $a_1 \geq 0$ so that the lapse stays non-negative near the root.

We note that we can compute the static mean curvature evaluated at the puncture by rearranging the Bona-Massó equation (4.8) as

$$K_0(R_0) = \lim_{R \to R_0} \frac{\beta^R \alpha'}{\alpha f(\alpha)} = \lim_{\alpha \to 0} \frac{\sqrt{-F(R_0)}\, a_1}{\alpha f(\alpha)}, \tag{4.28}$$

where we have used relation (3.13a) in the second equality. Evidently, whether or not $K_0(R_0)$ is finite depends on the behavior of $\alpha f(\alpha)$ as $\alpha \to 0$, which we have not yet evaluated in Eq. (4.28).

## The Isotropic Radius

We transform the Schwarzschild areal radius $R$ to the *isotropic radius $r$* by comparing the spatial part of the line element (1.3),

$$dl^2 = \gamma_{RR}\, dR^2 + R^2\, d\Omega^2 = \alpha^{-2}\, dR^2 + R^2\, d\Omega^2\,, \tag{4.29}$$

where we have used relation (3.13b), with the spatial line element in isotropic coordinates,

$$dl^2 = \psi^4\big(dr^2 + r^2\,d\Omega^2\big), \tag{4.30}$$

where $\psi$ is a so-called conformal factor. The metric (4.30) does not distinguish between the radial and angular elements $dr^2$ and $r^2\,d\Omega^2$. This representation readily translates to Cartesian coordinates as

$$dr^2 + r^2\,d\Omega^2 \propto \psi^{-4}\big(dx^2 + dy^2 + dz^2\big), \tag{4.31}$$

whereas the metric (4.29) does not. In general, isotropy gives $dl^2 = \psi^4 \eta_{ij}$, where $\eta_{ij}$ is a Euclidean metric (see, e.g., Exercise 1.5 in [12]). For this reason isotropic coordinates are often favored in codes that employ a 3D Cartesian grid.

By comparing (4.29) with (4.30) we obtain the system

$$\alpha^{-1}\,dR = \psi^2\,dr \tag{4.32a}$$

and

$$R = \psi^2 r. \tag{4.32b}$$

Dividing Eq. (4.32a) by Eq. (4.32b) yields

$$\frac{dr}{r} = \frac{dR}{R\alpha} = \frac{dR/d\alpha}{R}\frac{d\alpha}{\alpha}, \tag{4.33}$$

which gives us the integral

$$r = \exp\int \frac{dR/d\alpha}{R}\frac{d\alpha}{\alpha}. \tag{4.34}$$

25

Near the black-hole puncture we can make the leading-order approximations

$$\frac{dR}{d\alpha} \simeq \frac{1}{a_1} \quad (r \to 0) \tag{4.35}$$

and $R \simeq R_0$, allowing us to evaluate Eq. (4.34) as

$$r \propto \exp\left(\frac{1}{a_1 R_0} \ln \alpha\right) \quad (\alpha \to 0), \tag{4.36}$$

or equivalently,

$$\alpha \propto r^{1/\gamma} \quad (r \to 0) \tag{4.37}$$

where, as in [18], the exponent

$$\frac{1}{\gamma} \equiv a_1 R_0. \tag{4.38}$$

According to Eq. (4.37), if the exponent $1/\gamma$ is a non-negative integer $n$, derivatives of the lapse with respect to $r$ of order $n + 1$ and greater vanish at the puncture. However, if $1/\gamma$ is not an integer, derivatives of order $\lceil 1/\gamma \rceil$ and higher diverge at the puncture, producing numerical error. In particular, we are concerned with the behavior of $\partial^2 \alpha / \partial r^2$, which remains finite at the puncture so long as $1/\gamma$ is a non-negative integer.

For general values of $R > R_0$ (i.e. away from the puncture), we evaluate Eq. (4.34) numerically via the prescription set by Eqs. (46), (47), and (67) of [18] in order to compute $r(R)$. For consistency we confirm that the lapse behaves according to the power law (4.37); see also Eq. (56) in [18]. From Eq. (4.32b) we observe that the conformal factor

$$\psi = \sqrt{\frac{R}{r}} \propto r^{-1/2} \quad (r \to 0), \tag{4.39}$$

which is characteristic behavior for trumpet slices.

## 4.3 Results

### The Extremal Limit

Before discussing particular choices of the Bona-Massó function $f(\alpha)$, we consider extremal RN black holes with $Q = M \implies \lambda = 1$. For $\lambda = 1$, Eq. (4.15) becomes

$$\alpha^2 = \left(\frac{R - M}{R}\right)^2 + \frac{Ce^{2I(\alpha)}}{R^4}.$$
(4.40)

Since the exponential term is always positive, solutions for the lapse must have $C \leq 0$ in order to have a real root, independently of the integral $I(\alpha)$ (4.14).

As we note in Sec. 4.2, the procedure for locating the critical point depends on the behavior of $\alpha f(\alpha)$ in the limit $\alpha \to 0$. If $\alpha f(\alpha)$ remains finite near the puncture, the critical radius is a simultaneous root of Eqs. (4.23). For $\lambda = 1$, Eq. (4.23b) is

$$\left(1 - \frac{M}{R_c}\right)^2 + \alpha_c^2(f(\alpha_c) - 1) = 0.$$
(4.41)

Assuming $f(\alpha_c) > 1$, Eq. (4.41) implies that the only critical point for a non-negative $\alpha_c$ occurs at $R_c = M$ with $\alpha_c = 0$, for which Eq. (4.23a) has a root also. Evaluating Eq. (4.41) at this critical point gives $C = 0$ in the extremal limit.

For shock-avoiding slices, for which $\alpha f(\alpha)$ (4.27) diverges at the puncture, the critical lapse $\alpha_c = 0$ and the critical radius $R_c$ is a root of Eq. (4.23a). In the extremal limit, Eq. (4.23a) has roots $R_0 = M/2$ and $R_0 = M$. Only for the latter does the derivative $a_1$ (3.15) at the puncture take a non-imaginary value, such that we obtain exactly the same critical values as above for the other slices.

We therefore conclude that for all Bona-Massó functions $f(\alpha)$ considered here, we

have $C = 0$ in the extremal limit such that Eq. (4.41) yields

$$\alpha = \frac{R - M}{R} \quad (\lambda = 1), \tag{4.42}$$

from which follows

$$a_1 = \frac{1}{\gamma} = 1 \quad (\lambda = 1). \tag{4.43}$$

## $1 + \log$ Slices

For $f(\alpha) = k/\alpha$ (4.3), the integral (4.14) evaluates to

$$I(\alpha) = \frac{\alpha}{k}, \tag{4.44}$$

and hence Eq. (4.15) becomes

$$\alpha^2 = 1 - \frac{2M}{R} + \frac{Q^2}{R^2} + \frac{Ce^{2\alpha/k}}{R^4}. \tag{4.45}$$

Evaluating this equation at either the critical point or the root of the lapse yields two expressions for the constant of integration, namely

$$C = R^4 e^{-2\alpha_c/k} \left( \alpha_c^2 - 1 + \frac{2M}{R} - \frac{Q^2}{R_c^2} \right) = -R_0^4 + 2MR_0^3 - Q^2 R_0^2. \tag{4.46}$$

For these slices, Eq. (4.26) for the critical lapse becomes

$$0 = \lambda^2 \alpha_c^4 + 2k\lambda^2 \alpha_c^3 + \left( (k^2 + 2)\lambda^2 + 1 \right)\alpha_c^2 + k(3 - 2\lambda^2)\alpha_c + \lambda^2 - 1. \tag{4.47}$$

The analytical solutions to this quartic equation are unwieldy, so we locate the $1 + \log$ critical point numerically. The solution to Eq. (4.46) for the root $R_0$ is similarly unwieldy,

28

so we locate $R_0$ numerically also.

Next, we take the derivative of the lapse at the root by implicit differentiation of Eq. (4.45), which gives

$$2\alpha\alpha' = \frac{2M}{R^2} - \frac{2Q^2}{R^3} + C\left(\frac{2e^{2\alpha/k}\alpha'}{kR^4} - \frac{4e^{2\alpha/k}}{R^5}\right). \tag{4.48}$$

Collecting the $\alpha'$ terms gives

$$\left(2\alpha R^5 - \frac{2C}{k}e^{2\alpha/k}R\right)\alpha' = 2MR^3 - 2Q^2R^2 - 4Ce^{2\alpha/k}, \tag{4.49}$$

and we isolate $\alpha'$ as

$$\alpha' = \frac{2MR^3 - 2Q^2R^2 - 4Ce^{2\alpha/k}}{2\alpha R^5 - (2C/k)e^{2\alpha/k}R}. \tag{4.50}$$

Now evaluating at the root, i.e. setting $\alpha = 0$, we obtain

$$a_1 = -\frac{2MR_0^3 - 2Q^2R_0^2 - 4C}{(2C/k)R_0}; \tag{4.51}$$

the exponent (4.38) is then

$$\frac{1}{\gamma} = -\frac{2MR_0^3 - 2Q^2R_0^2 - 4C}{(2C/k)} \tag{4.52}$$

for these slices. Since Eq. (4.45) for $\alpha$ is transcendental, we obtain solutions $\alpha(R;\lambda)$ numerically for $k = 2$. Lastly, we transform from the areal radius $R$ to the isotropic radius $r$ (see Sec. 4.2) and plot $\alpha(r)$ for selected values of $\lambda$ in Fig. 4.1.
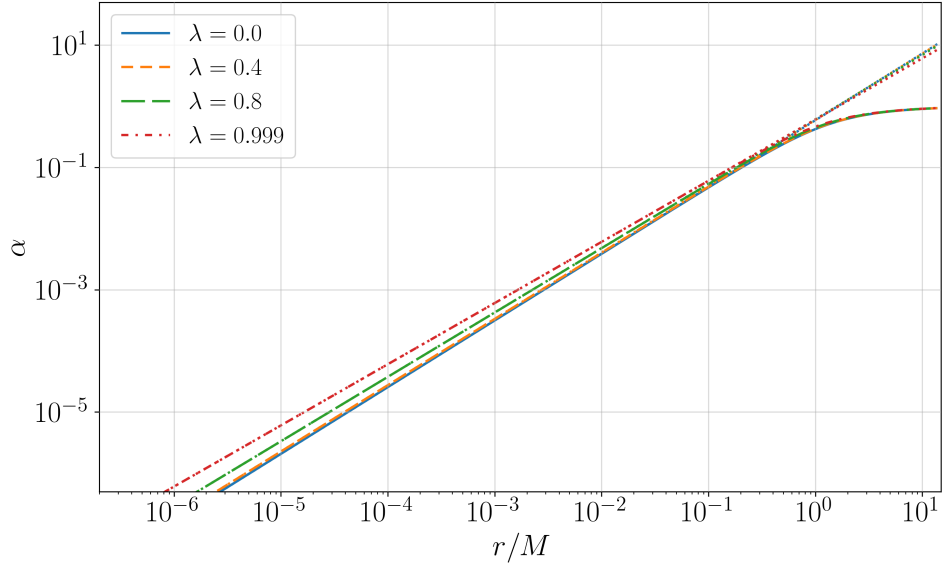
Figure 4.1: The numerical profile of the lapse $\alpha(r)$ for $\lambda \in \{0, 0.4, 0.8, 0.999\}$ for $1 + \log$ slices with $k = 2$. The dotted lines represent the expected power-law behavior $\alpha \propto r^{1/\gamma}$ in the limit $r \to 0$.

## Analytical Trumpet Slices

Next, we consider the trumpet slices given by $f(\alpha) = (1 - \alpha)/\alpha$ (4.4). For uncharged black holes, these slices are completely analytical [53]. For charged black holes, Eq. (4.26) for these slices is

$$0 = \frac{3}{1 - \alpha_c} - \lambda^2 - \frac{2}{(1 - \alpha_c)^2} + \frac{2}{(1 - \alpha_c)^2} \alpha_c^2. \tag{4.53}$$

Multiplying both sides by the term $(1 - \alpha_c)^2$ yields

$$0 = 3(1 - \alpha_c) - \lambda^2 (1 - \alpha_c)^2 - 2 + 2\alpha_c^2 = (2 - \lambda^2)\alpha_c^2 - (3 - 2\lambda^2)\alpha_c + 1 - \lambda^2. \tag{4.54}$$

This quadratic for the critical lapse has roots

$$\alpha_c = \frac{3 - 2\lambda^2 \pm \sqrt{(2\lambda^2 - 3)^2 - 4(2 - \lambda^2)(1 - \lambda^2)}}{2(2 - \lambda^2)} = \frac{3 - 2\lambda^2 \pm 1}{4 - 2\lambda^2}; \qquad (4.55)$$

evidently, choosing "+" in Eq. (4.55) gives $\alpha_c = 1$ and therefore $R_c = \infty$, meaning the slice avoids a critical point up to the asymptotic limit. Here we focus on slices whose critical point lies within the outer horizon, so we instead choose the "−" solution to yield

$$\alpha_c = \frac{1 - \lambda^2}{2 - \lambda^2}, \qquad (4.56)$$

whose corresponding critical radius (4.25) is

$$R_c = M(2 - \lambda^2). \qquad (4.57)$$

This agrees with the uncharged limit $(R_c, \alpha_c) \to (2M, 0.5)$ as $\lambda \to 0$ considered in [52].

The integral (4.14) evaluates to

$$I(\alpha) = -\ln(1 - \alpha), \qquad (4.58)$$

so Eq. (4.15) becomes

$$\alpha^2 = 1 - \frac{2M}{R} + \frac{Q^2}{R^2} + \frac{C}{R^4(1 - \alpha)^2}, \qquad (4.59)$$

and thus, via Eqs. (4.57) and (4.56), the constant of integration

$$C = M^4(1 - \lambda^2). \qquad (4.60)$$

With the above, Eq. (4.59) yields a quartic equation for the root $R_0$ with two real solutions,

31

one of which is $R_0 = M$. Taking a radial derivative of Eq. (4.59), we have

$$2\alpha\alpha' = \frac{2M}{R^2} - \frac{2Q^2}{R^3} + C\left(\frac{2\alpha'}{R^4(1-\alpha)^3} - \frac{4}{R^5(1-\alpha)^2}\right). \tag{4.61}$$

Grouping the $\alpha'$ terms,

$$2\left(R^5\alpha - \frac{CR}{(1-\alpha)^3}\right)\alpha' = 2MR^3 - 2Q^2R^2 - \frac{4C}{(1-\alpha)^2}, \tag{4.62}$$

so $\alpha'$ is given by

$$\alpha' = \frac{MR^3 - Q^2R^2 - 2C/(1-\alpha)^2}{R^5\alpha - CR/(1-\alpha)^3}. \tag{4.63}$$

Evaluating this at the root of the lapse and inserting Eq. (4.60) yields

$$a_1 = \frac{MR_0^2 + Q^2R_0}{M^4(1-\lambda^2)} + \frac{2}{R_0}, \tag{4.64}$$

from which we observe that $R_0 = M$ is the only root for which $a_1 > 0$. In particular, for $R_0 = M$, we have $a_1 = 1/M$ and hence $1/\gamma = 1$. These results are independent of the charge-to-mass ratio.

Substituting Eq. (4.60) back into Eq. (4.59), we obtain two real solutions for the lapse as a function of the areal radius. However, only the solution

$$\alpha(R) = \frac{R - M}{R} \tag{4.65}$$

satisfies $\alpha' > 0$ for all $R$. This solution is identical to the extremal solution (4.42) but, remarkably, holds for all $\lambda$ and not just $\lambda = 1$. To check this result, we consider the limit $a \to 0$ and $\Lambda \to 0$, where $a$ is the rotation parameter and $\Lambda$ the cosmological constant, of the analytical trumpet slices of Kerr-Newman-de Sitter (KNdS) spacetimes that Dennison, Baumgarte, and Montero (2014) [59] constructed. The KNdS spacetime

represents a spinning, charged black hole in the presence of the cosmological constant. For RN spacetimes with $R_0 = M$, the line element (26) in [59] reduces to

$$ds^2 = -F\,dt^2 + 2M\frac{\sqrt{1-\lambda^2}}{R-M}\,dt\,dR + \frac{R^2}{(R-M)^2}\,dR^2 + R^2\,d\Omega^2 \qquad (4.66)$$

with $F$ given by Eq. (4.7). Comparing this with the $3+1$ line element (1.3), we identify the $RR$-component of the spatial metric

$$\gamma_{RR} = \frac{R^2}{(R-M)^2}, \qquad (4.67)$$

from which we compute the shift

$$\beta^R = \gamma_{RR}^{-1}\frac{M}{R-M}\sqrt{1-\lambda^2} = \frac{M(R-M)\sqrt{1-\lambda^2}}{R^2}. \qquad (4.68)$$

The lapse is then given by

$$\alpha^2 = \gamma_{RR}\left(\beta^R\right)^2 + F = \frac{M^2-Q^2}{R^2} + 1 - \frac{2M}{R} + \frac{Q^2}{R^2} = \frac{M^2+R^2-2MR}{R^2} = \frac{(M-R)^2}{R^2};$$
$$(4.69)$$

taking the positive root, we recover

$$\alpha = \frac{R-M}{R}, \qquad (4.70)$$

corroborating the solution (4.65). We convert this solution to isotropic coordinates and plot the result $\alpha(r)$ in Fig. 4.2.
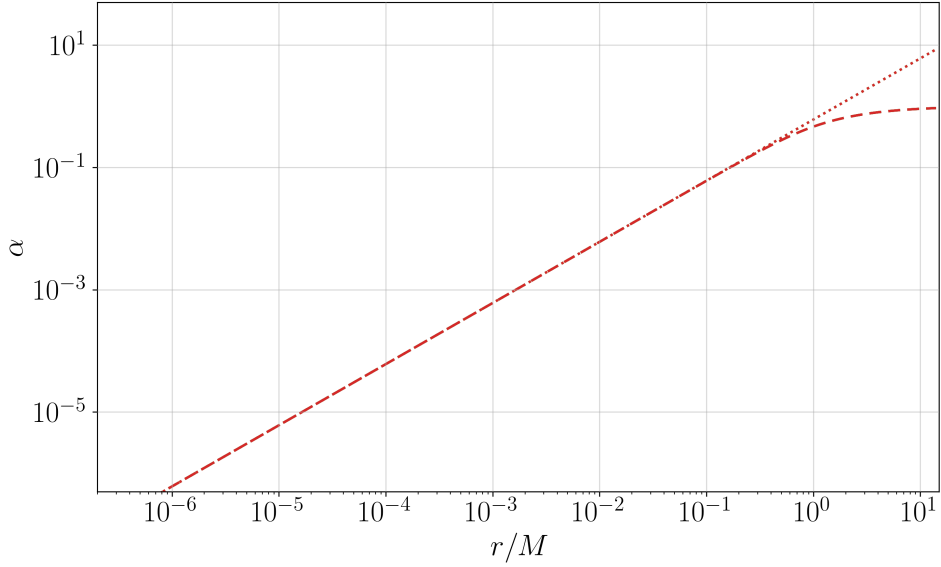
Figure 4.2: The analytical profile of the lapse $\alpha(r)$ for analytical trumpet slices does not depend on the black-hole charge.

As an example of the utility of analytical trumpet slices, we can use the analytical solution for the lapse (4.65) to compute the height function directly for the uncharged case $\lambda = 0$. Substituting Eq. (4.65) into Eq. (3.12a) and solving for $h'(R)$, we obtain

$$h'(R) = \frac{\sqrt{\alpha^2 - F}}{\alpha F} = \frac{MR}{\sqrt{(R-M)^2(R-2M)^2}} \quad (\lambda = 0), \tag{4.71}$$

where we have taken a positive square root. Integration then yields

$$h(R) = M \ln \frac{2(R-2M)}{(R-M)} \quad (\lambda = 0), \tag{4.72}$$

where we have arbitrarily chosen a constant of integration so that $h(3M) = 0$. Note that $h(R)$ diverges logarithmically both at the puncture $R_0 = M$ and the horizon $R = 2M$. This behavior is evident in Fig. 5.2, which also illustrates a hypothetical perturbation for dynamical slices, the subjects of Ch. 5.

## Shock-Avoiding Slices

We now choose $f(\alpha) = 1 + \kappa/\alpha^2$ (4.5). Alcubierre [54] proposed the resulting slices as alternatives to $1 + \log$ slices that avoid gauge shocks. For this choice, Eq. (4.22) becomes

$$\alpha' = \frac{\alpha^2 + \kappa}{\alpha R} \frac{2 - 3M/R + Q^2/R^2 - 2\alpha^2}{1 - 2M/R + Q^2/R^2 + \kappa}.$$

(4.73)

As we discussed in Sec. (4.2), the denominator (4.23b) of the right-hand side of this expression now vanishes for $\alpha = 0$. For $\alpha = 0$ the numerator (4.23a) has a root at the critical radius

$$R_c = R_0 = \frac{3 + \sqrt{9 - 8\lambda^2}}{4} M,$$

(4.74)

where we have chosen the outermost solution. Of course, this critical point, coinciding with the root of the lapse, may not be the only critical point through which $\alpha(R)$ passes. It is possible that the denominator of the second factor on the right-hand side of Eq. (4.73) vanishes at a radius $R_c^* > R_c$; setting this quadratic expression to zero, we compute

$$R_c^* = \frac{1 + \sqrt{1 - \lambda^2(1 + \kappa)}}{1 + \kappa} M,$$

(4.75)

which we note is real only for $\kappa \leq \lambda^{-2} - 1$. Substituting this alternative value into Eq. (4.23a), we determine the corresponding critical lapse

$$\alpha_c^* = \left( -1 + \sqrt{1 - \lambda^2(\kappa + 1)} - \lambda^2(\kappa + 1) \right)^{1/2} \frac{1}{\sqrt{2}\lambda}.$$

(4.76)

We observe that if $\kappa$ satisfies

$$\kappa > 1 - \frac{3 - \sqrt{9 - 8\lambda^2}}{2\lambda^2}$$

(4.77)

then no real solutions for $\alpha_c^*$ exist. We thus conclude that, in this case, the critical point is given by Eq. (4.74) and $\alpha_c = 0$.

We assume from here that condition (4.77) holds for all $\alpha_c = 0$. As in [52], we may evaluate the integral (4.14) to obtain

$$I(\alpha) = \frac{1}{2} \ln \left( \frac{\alpha^2 + \kappa}{\kappa} \right), \tag{4.78}$$

so that Eq. (4.15) becomes

$$\alpha^2 = 1 - \frac{2M}{R} + \frac{Q^2}{R^2} + \frac{\alpha^2 + \kappa}{\kappa} \frac{C}{R^4}. \tag{4.79}$$

Solving for the constant of integration yields

$$C = -R_c^4 \left( 1 - \frac{2M}{R_c} + \frac{Q^2}{R_c^2} \right); \tag{4.80}$$

with $R_c$ given by Eq. (4.74), we then have

$$C = M^4 \left( \frac{27}{32} + \frac{(9 - 8\lambda^2)^{3/2}}{32} - \frac{9\lambda^2}{8} + \frac{\lambda^4}{4} \right). \tag{4.81}$$

For Schwarzschild spacetimes, i.e. for $\lambda = 0$, we recover $C = 3^3/2^4$ as found by [52].

To evaluate the derivative $a_1$, we apply L'Hôpital's rule to Eq. (4.73):

$$\begin{aligned}
\lim_{\alpha \to 0} \alpha' &= \lim_{\alpha \to 0} \frac{(d/dR)((\alpha^2 + \kappa)(2 - 3M/R + Q^2/R^2 - 2\alpha^2))}{(d/dR)(\alpha R(1 - 2M/R + Q^2/R^2 + \kappa))} \\
&= \frac{1}{\lim\limits_{\alpha \to 0} \alpha'} \frac{\kappa(4R_0 - 3M)}{(1 + \kappa)R_0^3 - 2MR_0^2 + Q^2 R_0}. \tag{4.82}
\end{aligned}$$

Now imposing $\alpha' \to a_1$ as $\alpha \to 0$, multiplying both sides by $a_1$, and taking a positive root,

we obtain

$$a_1 = \sqrt{\frac{\kappa(4R_0 - 3M)}{(1+\kappa)R_0^3 - 2MR_0^2 + Q^2 R_0}}. \tag{4.83}$$

Then using Eq. (4.74), the exponent

$$\frac{1}{\gamma} = \left(\frac{18 + 6\sqrt{9 - 8\lambda^2} - 16\lambda^2}{9\kappa + (3\kappa - 1)\sqrt{9 - 8\lambda^2} + 4\lambda^2(1 - \kappa) - 3}\right)^{1/2}\sqrt{\kappa}, \tag{4.84}$$

and we verify that we recover

$$\frac{1}{\gamma} = \sqrt{\frac{6\kappa}{3\kappa - 1}} \tag{4.85}$$

for $\lambda = 0$ as in [52]. In the extremal case $\lambda = 1$, Eq. (4.84) reduces to $1/\gamma = 1$ independently of $\kappa$, as expected from our discussion in Sec. 4.3.

Substituting Eq. (4.81) into Eq. (4.79), we obtain an analytical solution for the lapse

$$\alpha(R) = \left(\frac{32R^4 - 64MR^3 + 32Q^2R^2 + A}{32\kappa R^4 - A}\right)^{1/2}\sqrt{\kappa}, \tag{4.86}$$

where we abbreviate

$$A \equiv 27M^4 + M^4\left(9 - 8\lambda^2\right)^{3/2} - 36M^2Q^2 + 8Q^4. \tag{4.87}$$

We use the above solution to transform to isotropic coordinates as discussed in Sec. 4.2 and show results for $\alpha(r)$ with $\kappa = 1$ in Fig. 4.3.
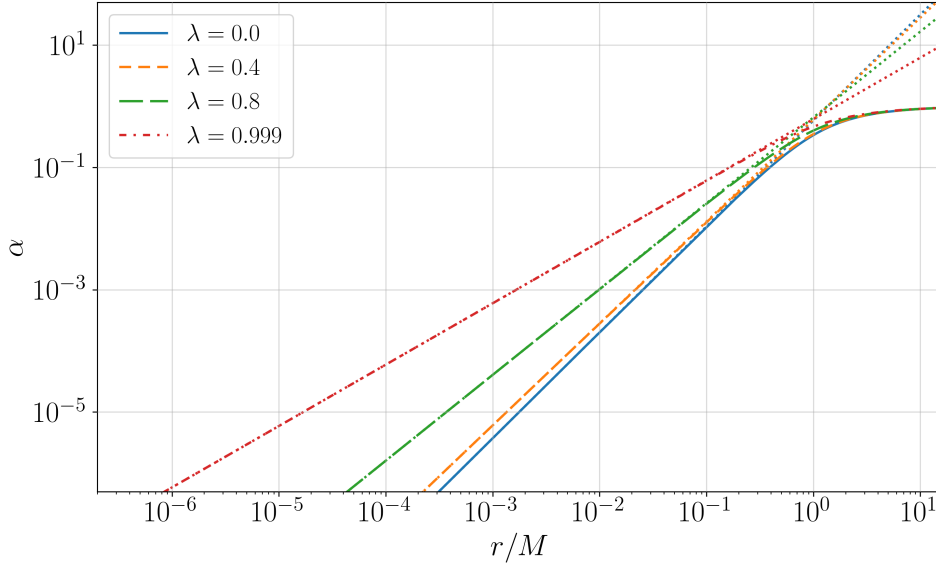
Figure 4.3: The analytical profile of the lapse $\alpha(r)$ via Eq. (4.86) for $\lambda \in \{0, 0.4, 0.8, 0.999\}$ for shock-avoiding slices with $\kappa = 1$.

## Zero Order Shock-Avoiding Slices

The shock-avoiding slicing condition given by Eq. (4.5) has the unusual property that it allows the lapse to become negative. We thus also study slices that avoid shocks to leading order only and do not allow $\alpha < 0$ (see, e.g., [60, 61] for numerical applications). These zero order shock-avoiding slices are given by $f(\alpha) = a_0^2/(2\alpha + (a_0 - 2)\alpha^2)$ (4.6). We note that $1 + \log$ slicing (4.3) with $k = 2$ corresponds to Eq. (4.6) with $a_0 = 2$.

As in [52] we can compute the integral (4.14) analytically, yielding

$$I(\alpha) = \frac{\alpha}{2a_0^2}(4 - (a_0 - 2)\alpha), \tag{4.88}$$

and we may then evaluate the derivative of the lapse at its root,

$$a_1 = a_0 \frac{-2MR_0^3 + 2Q^2R_0^2 + 4C}{4CR_0}; \tag{4.89}$$

38

however, expressions for the critical values, constant $C$, and root $R_0$ are unwieldly, so we compute these numerically. Then using these results we apply numerical root-finding to Eq. (4.15), transform to the isotropic radius $r$ numerically, and plot $\alpha(r)$ for $a_0 = 4/3$ in Fig. 4.4.
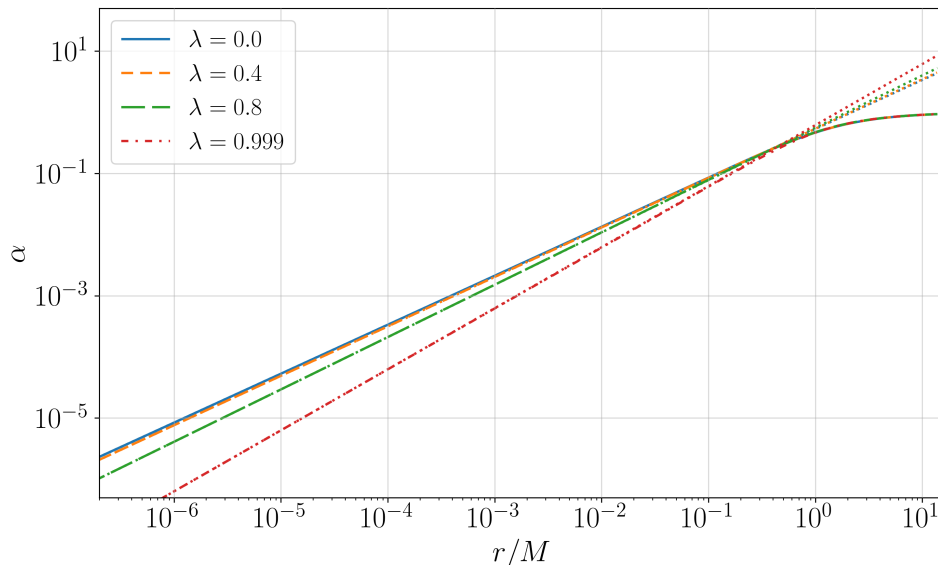


Figure 4.4: The numerical profile of the lapse $\alpha(r)$ for $\lambda \in \{0, 0.4, 0.8, 0.999\}$ for zero order-shock avoiding slices with $a_0 = 4/3$.

## Summary of Results

In Fig. 4.5 we compare our results for the critical lapse, constant of integration, and exponent $1/\gamma$ as a function of the black-hole charge-to-mass ratio $\lambda$ for the four slicing conditions considered in this chapter. In Fig. 4.6 we plot values for the critical radii and roots $R_0$ of the lapse against $\lambda$ for each of these conditions. In Figs. 4.7–4.10 we compare profiles of the lapse $\alpha(r)$ for these slices with particular values of $\lambda$.

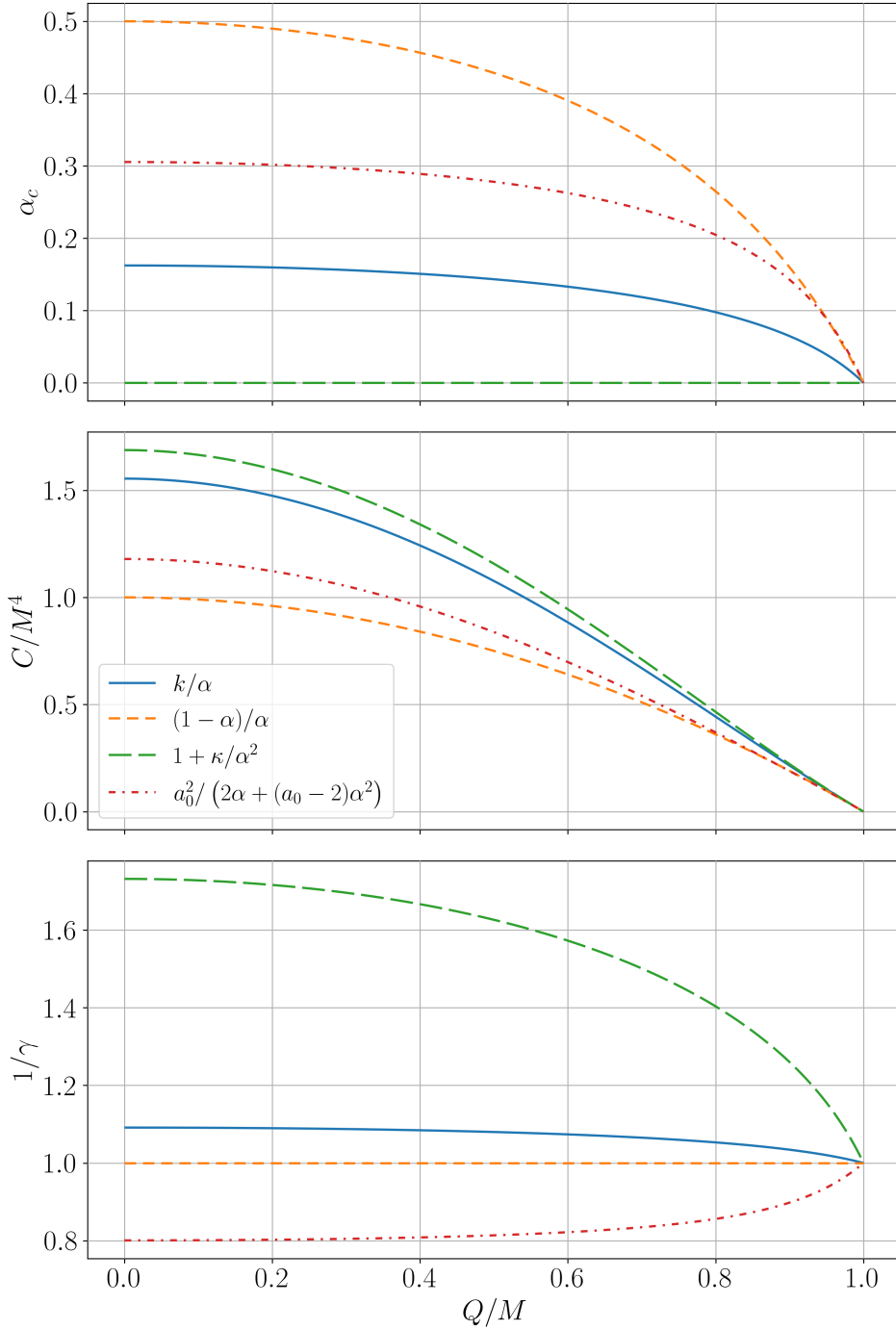Figure 4.5: The critical lapse $\alpha_c$ (top), constant of integration $C$ (center), and exponent $1/\gamma$ (bottom) plotted against the black-hole charge-to-mass ratio $\lambda$ (up to 0.999) on a shared horizontal axis for each of the $f(\alpha)$ we consider. The solid (blue) line corresponds to $1 + \log$ slices (with $k = 2$), the short-dashed (orange) line to analytical trumpet slices, the long-dashed (green) line to fully shock-avoiding slices (with $\kappa = 1$), and the dash-dotted (red) line to zero order shock-avoiding slices (with $a_0 = 4/3$). All slices have the same critical values in the extremal limit $\lambda \to 1$.

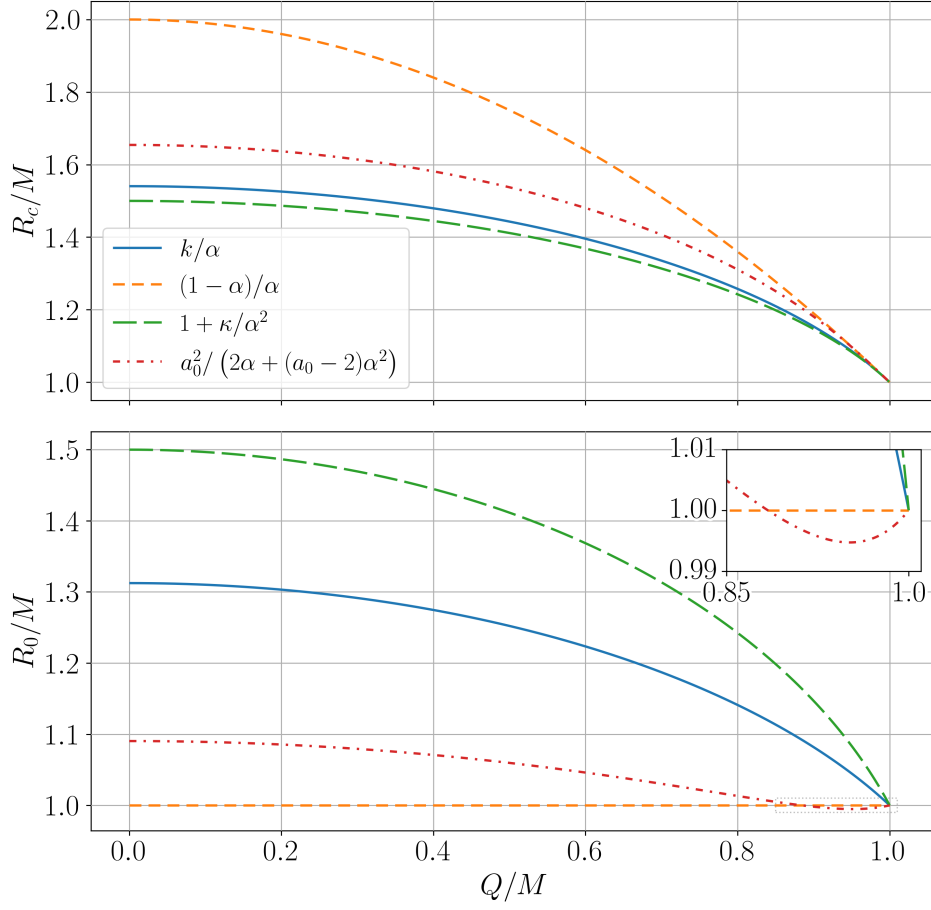Figure 4.6: The critical areal radius $R_c$ (top) and the root $R_0$ of the lapse (bottom) versus $\lambda$ for each of the $f(\alpha)$ we consider. The inset in the top-right corner of the bottom panel shows an expanded view of the bottom-right region, where the root of the lapse for zero order shock-avoiding slices falls slightly below $R_0 = M$ near the extremal limit $\lambda \to 1$.
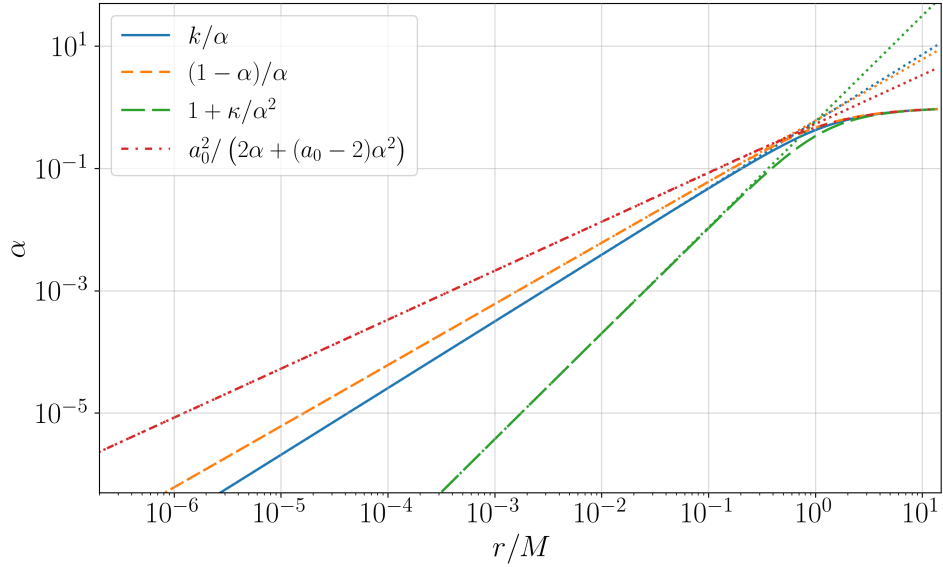
Figure 4.7: Profiles of the lapse $\alpha$ as a function of isotropic radius $r$ for each of the slicing conditions we consider (with $k = 2$, $\kappa = 1$, and $a_0 = 4/3$) with charge-to-mass ratio $\lambda = 0$ (the Schwarzschild spacetime). See Fig. 4.1 for an explanation of the dotted lines.
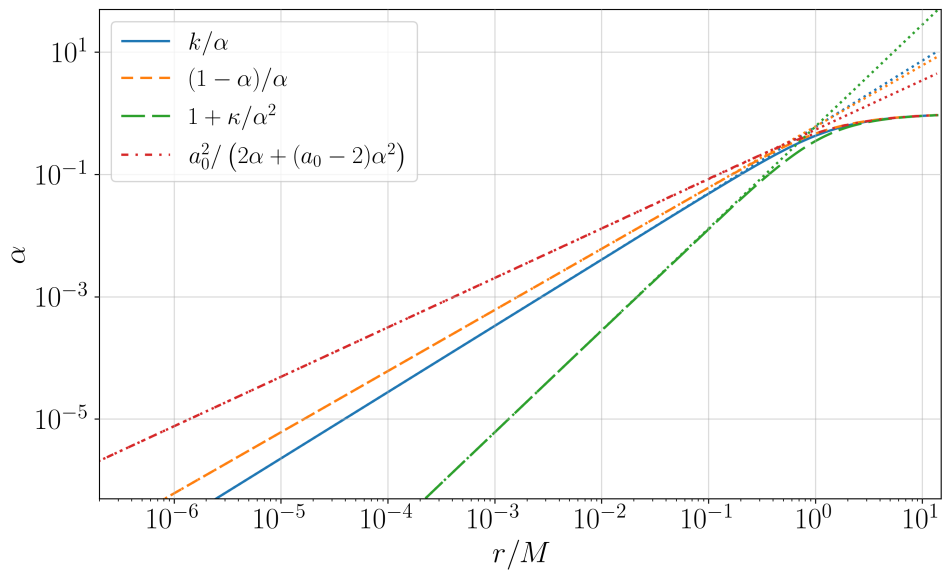


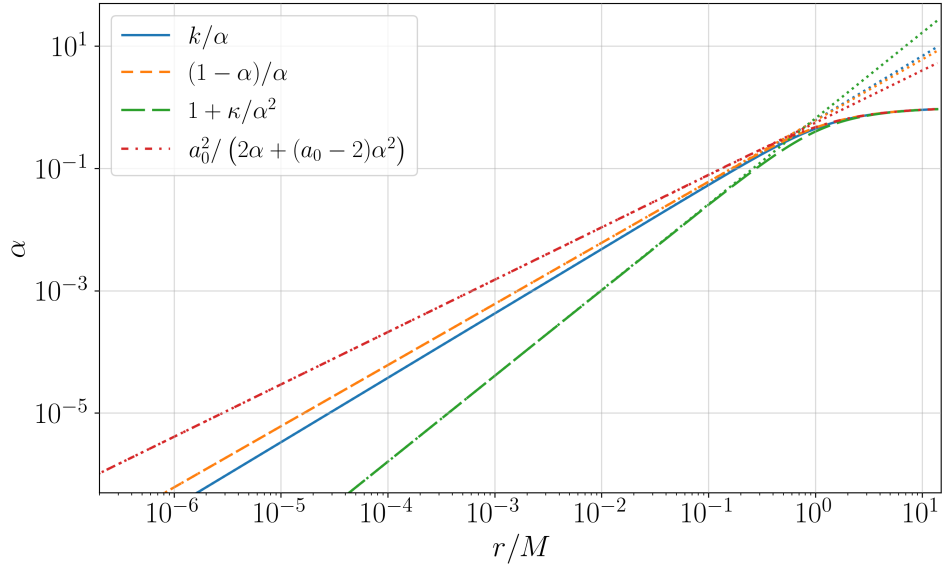Figure 4.8: Same as Fig. 4.7 but with $\lambda = 0.400$.

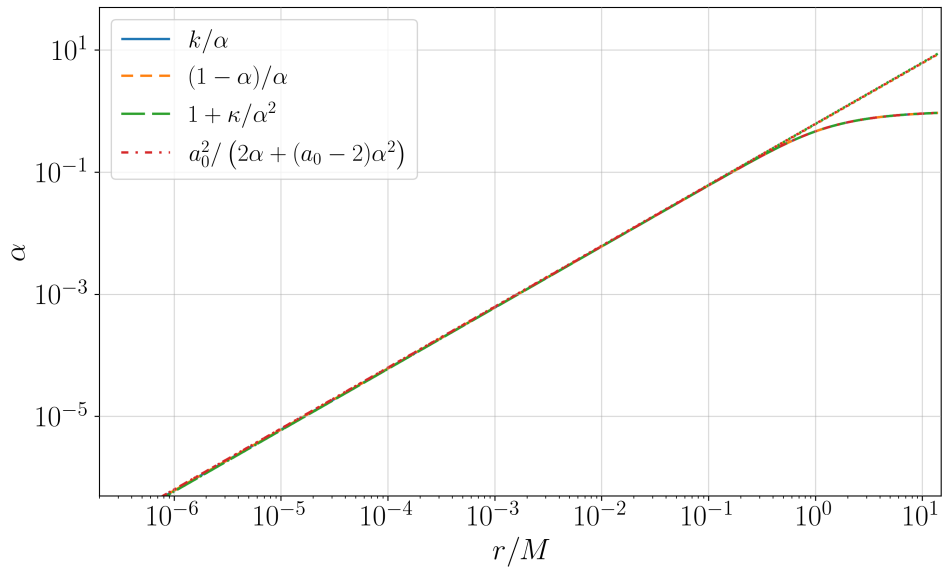Figure 4.9: Same as Fig. 4.7 but with $\lambda = 0.800$.



Figure 4.10: Same as Fig. 4.7 but with $\lambda = 0.999$.

In general we observe that in the extremal limit $\lambda \to 1$, all slices converge to a unique slice that is independent of the choice of Bona-Massó function, as anticipated in Sec. 4.3. The lapse for this unique extremal slice is given by that of the analytical trumpet slices (4.65) of Sec. 4.3, which we derived without assuming $\lambda = 1$. We also note that in the asymptotic limit $r \to \infty$, i.e. toward Minkowski space, all lapse profiles converge to unity as expected.

# 5 Dynamical Bona-Massó Slices

This chapter discusses the collaborative work of Li, Baumgarte, Dennison, and de Oliveira (2023) [62] in additional detail.

## 5.1 Motivation

In Ch. 4 we computed properties of Bona-Massó slices of RN spacetimes in static equilibrium, i.e. we studied the limiting characteristics of these slices in the spatial domain as $t \rightarrow \infty$. However, in GR we are interested in how systems governed by the Einstein equations (1.1) evolve over time, and therefore in numerical relativity we are interested in how spacetime slices behave as they are evolved and not just the static equilibria to which they eventually settle. In Ch. 4 we were motivated to study the shock-avoiding slices given by Eq. (4.5) precisely *because* of their dynamical behavior, namely their avoidance of gauge shocks that can arise over the course of time evolution in $1 + \log$ slices. Baumgarte and Hilditch (2022) [57] showed that, although shock-avoiding slices sometimes allow the lapse to become negative, they exhibit stability and accuracy comparable to that of $1 + \log$ slices in test simulations of black holes, neutron stars, and gravitational collapse. One such test evolved a Schwarzschild black hole using the Bona-Massó slicing condition (4.1) starting with a slice of constant Schwarzschild time. In Fig. 5.1, adapted from [57], the lapse at the black-hole puncture is plotted against time for $1 + \log$ slices (with $k = 2$) and shock-avoiding slices (with $\kappa = 1$ and $\kappa = 2/3$). Whereas in Ch. 4 we use $\alpha_c$ to denote the *critical* lapse, in this chapter $\alpha_c$ refers to the *central* lapse, i.e. at isotropic
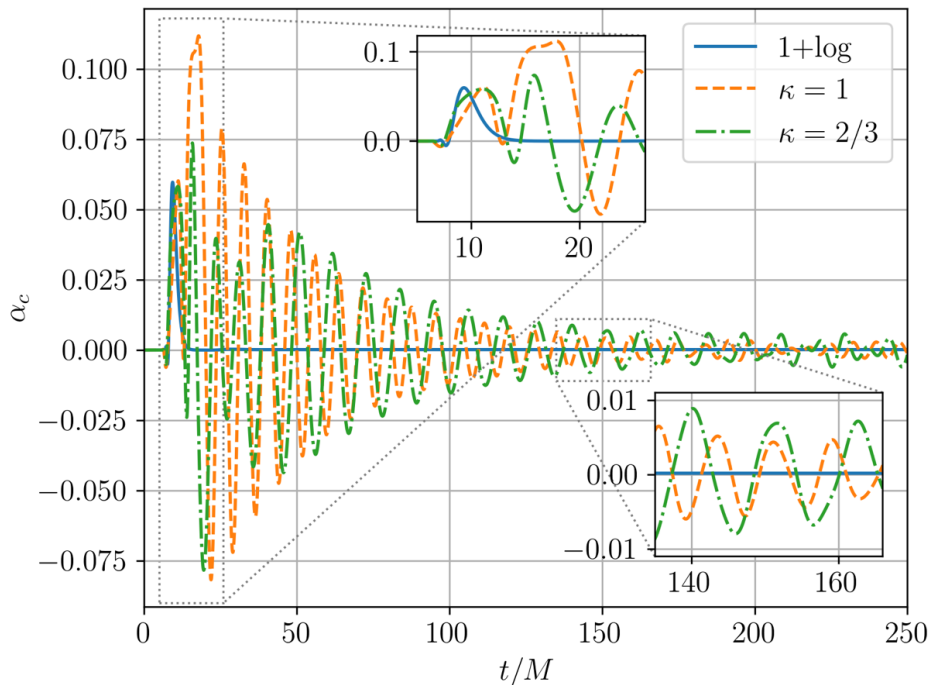
45

Figure 5.1: The central lapse $\alpha_c$ at the black-hole puncture in the evolution of a single Schwarzschild black hole with the Bona-Massó slicing condition (4.1). Adapted from Fig. 2 of [57].

radius $r = 0$. For dynamical slices the central lapse may be nonzero during evolution; in the limit $t \to \infty$, however, $\alpha_c$ settles to zero, and hence for static slices we identify the location of the black-hole puncture with the root of the lapse. Here the black-hole puncture corresponds simply to the center $r = 0$ of the isotropic coordinate system (see Sec. 4.2); this coincides exactly with the root $R_0$ of the lapse for static slices only.

As Fig. 5.1 makes apparent, the central lapse for shock-avoiding slices exhibits both quantitative and qualitative differences in its behavior compared to $\alpha_c$ for $1 + \log$ slices. Whereas for $1 + \log$ slices the lapse appears to decay roughly exponentially after a short period ($\sim 8M$), for shock-avoiding slices the lapse appears to undergo harmonic oscillation. At early times (up to $\sim 150M$) these oscillations appear damped, but at later times, the amplitude remains mostly constant. We observe also that the period of oscillations is larger for a smaller value of the constant $\kappa$ in Eq. (4.5).

We caution that neither the observation of exponential decay nor harmonic oscillation is exact. We also note that numerical error due to finite-differencing across the black-hole puncture is large enough to prevent pointwise convergence. However, an independent code based on a multidomian spectral method (see [63]) produced the same qualitative behavior in $\alpha_c$ as with the finite difference method, namely exponential decay for $1 + \log$ slices and harmonic oscillation for shock-avoiding slices, albeit with some quantitative differences.

The observed exponential decay suggests a first-order ordinary differential equation (ODE) governs $\alpha_c$ for $1 + \log$ slices, whereas the observed harmonic oscillation suggests a second-order ODE governs $\alpha_c$ for shock-avoiding slices. Since both the $1 + \log$ and shock-avoiding slicing conditions are imposed by the same equation, namely the Bona-Massó condition (4.1), the origin of this qualitative contrast is mysterious. In this chapter we seek analytical insight into what causes this difference in behavior. We employ a dynamical height-function approach (see Ch. 3) to represent time-dependent coordinate transformations of spacetimes whose metric[1] takes the form (3.2) and explore the behavior of the central lapse.

## 5.2   Methods

We study dynamical slices in the limit that they may be considered linear perturbations of their static counterparts of Ch. 4. Since we expect the static height function to diverge at the black-hole puncture and the outer horizon (see Sec. 4.3) and to asymptote to a finite value toward spatial infinity, these perturbations require different treatments in different regimes. As Fig. 5.2 illustrates, far from the black hole, where the slope $h'_0(R)$ of the static "background" decreases monotonically, we may describe the dynamical slice in terms of a perturbation $\eta(t, R)$ of the height function $h_0(R)$ itself, i.e. $h(t, R) = h_0(R) + \eta(t, R)$. We

---

[1]Since the coefficient $F(R)$ is kept general, this analysis works identically for RN and Schwarzschild spacetimes.

will recover well-known wave equations for the lapse in this limit. Close to the puncture, however, $h_0$ and its derivative diverge, so that changes in $h$ may also diverge. In this region it is more natural to describe the slice in terms of a small shift $\rho(t, R)$ in the radial coordinate $R$ where we evaluate the background height function. We will use this approach to arrive at our main result concerning the dynamical behavior beget by different slicing conditions at the black-hole puncture.
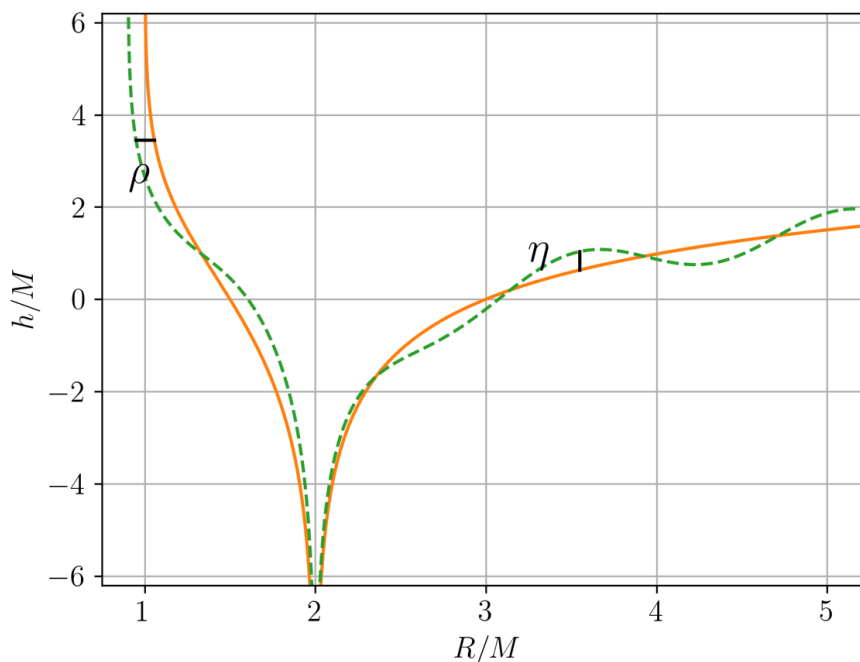


Figure 5.2: Graph of the static height function $h_0(R)$ for the analytical trumpet slice together with a hypothetical perturbation. The perturbation can be described by changes $\eta$ in $h$ far from the puncture and changes $\rho$ in $R$ close to the static puncture at $R_0 = M$.

## Perturbations in the Far Limit

In the far limit $R \gg M$, where we assume $h_0' \to 0$, we describe the perturbation as

$$h(t, R) = h_0(R) + \eta(t, R). \tag{5.1}$$

Given our assumption $h_0' \ll 1$, we may write $\dot{h} = \dot{\eta}$ and $h' \simeq \eta'$. Since $F \simeq 1$ also in this regime, Eqs. (3.8), (3.6), and (3.11) give, to leading order in the perburbation $\eta$,

$$\alpha \simeq 1 - \dot{\eta}, \quad \beta^R \simeq \eta', \quad \text{and} \quad K \simeq \eta'' + \frac{2}{R}\eta' = \nabla^2 \eta, \tag{5.2}$$

where in the last equality we have recognized that the Laplacian in spherical symmetry is

$$\nabla^2 = \frac{1}{R^2}\partial_R(R^2\partial_R) = \partial_R^2 + \frac{2}{R}\partial_R.$$

Substituting these expressions into the Bona-Massó equation (4.1), we obtain a wave equation for the pertubation $\eta$,

$$-\ddot{\eta} + f(1)\nabla^2\eta = 0, \tag{5.3}$$

where $f(1)$ denotes the Bona-Massó function $f(\alpha)$ evaluated at $\alpha = 1$. By Eqs. (5.2), taking a time derivative of Eq. (5.3) yields a wave equation for the lapse,

$$\ddot{\alpha} - f(1)\nabla^2\alpha = 0. \tag{5.4}$$

We thus conclude that in the far limit, dynamical perturbations in the lapse travel at speeds $v = \sqrt{f(1)}c$, where we have written the speed of light $c$ for clarity. For $1 + \log$ slicing given by Eq. (4.3) with $k = 2$, $f(1) = 2$; this confirms the well-known result that gauge modes travel at a speed $v = \sqrt{2}c$. For shock-avoiding slices given by Eq. (4.5), gauge modes travel at a speed $v = \sqrt{1 + \kappa}c$ (see, e.g., [54, 55]).[2]

---

[2]Recall that the above waves describe pure gauge modes, so that a wave speed $v > c$ does not violate causality.

## Perturbations at the Puncture

We now turn to perturbations close to the black-hole puncture. In this regime, where $h_0$ and its derivative diverge, a perturbative ansatz like Eq. (5.1) cannot represent a perturbation like the one sketched in Fig. 5.2, i.e. one that shifts the puncture to a new radial coordinate, with $\eta < \infty$. Rather, we describe perturbations in the vicinity of the puncture in terms of a dynamical radial perturbation $\rho(t, R)$. In particular, we will equate the perturbed height function $h(t, R)$ with the static height function $h_0$ evaluated at a radius

$$\tilde{R} = R + \rho(t, R) \tag{5.5}$$

as sketched in Fig. 5.2, with $\rho$ given by

$$h(t, R) = h_0(\tilde{R}) = h_0(R + \rho). \tag{5.6}$$

Derivatives of $h$ are then given by

$$\dot{h}(t, R) = h_0'(\tilde{R})\dot{\rho}(t, R) \quad \text{and} \quad h'(t, R) = h_0'(\tilde{R})(1 + \rho'(t, R)). \tag{5.7}$$

Substituting Eqs. (5.7) into Eqs. (3.4), (3.6), and (3.8), we obtain

$$\gamma_{RR} = F^{-1}\left(1 - F^2 h_0'^2 (1 + \rho')^2\right) \tag{5.8}$$

for the radial metric component,

$$\beta^R = \frac{F^2(1 - h_0'\dot{\rho})h_0'(1 + \rho')}{1 - F^2(h_0')^2(1 + \rho')^2} \tag{5.9}$$

for the radial shift component, and

$$\alpha^2 = \frac{(1 - h_0'\dot\rho)^2 F}{1 - F^2 h_0'^2 (1 + \rho')^2} \tag{5.10}$$

for the lapse. We observe from Eq. (5.8) that $\gamma_{RR}$ diverges where $h_0'(\tilde R)$ diverges.

Whereas for static slices, the divergence of $h_0$ necessarily coincides with a root of the lapse, this is not true in general for dynamical slices. However, even for dynamical slices, we identify the black-hole puncture as the place where the spatial metric component $\gamma_{RR}$ diverges. According to Eq. (3.4), this coincides with a divergence of the height function $h$ at $R < 2M$. We may therefore identify the black-hole puncture with a divergence of $h_0'$ at $\tilde R = R_0$ as discussed in Sec. 3.2, except that it is now located at $R = R_0 - \rho$. Evaluating the lapse (5.10) at the puncture, i.e. in the limit $h_0' \to \infty$, we obtain

$$\alpha = \frac{\dot\rho}{\sqrt{-F}(1 + \rho')}, \tag{5.11}$$

while the shift (5.9) becomes

$$\beta^R = \frac{\dot\rho}{1 + \rho'}. \tag{5.12}$$

We now introduce the derivative along the normal vector

$$\partial_n \equiv \alpha n^a \partial_a = \partial_t - \beta^R \partial_R, \tag{5.13}$$

allowing us to rewrite Eqs. (5.11) and (5.12) in the more compact form

$$\alpha = (-F)^{-1/2}\partial_n \rho \quad \text{and} \quad \beta^R = \partial_n \rho. \tag{5.14}$$

Unlike in the static case [see Eq. (3.12a)], the lapse does *not* necessarily vanish at the puncture for time-dependent slices, as has been observed in many numerical simulations

(see, e.g., Fig. 5.1).

We now evaluate the Bona-Massó condition (4.1) at the puncture. Substituting the dynamical lapse (5.10) and shift (5.9) into Eq. (3.11) for the mean curvature and evaluating the result at the puncture, where $h_0' \to \infty$ and $\tilde{R} = R_0$, we obtain

$$K = -\frac{4F + RF'}{2R\sqrt{-F}}. \tag{5.15}$$

In the above, the metric coefficient $F$ and its derivative are evaluated at a radius $R = R_0 - \rho$. For $\rho \ll R_0$, we may expand about $\tilde{R} = R_0$ and rewrite (5.15) as

$$K(R) \simeq K(R_0) - \rho K'(R_0), \tag{5.16}$$

where $K' = dK/dR$. Then using expressions (5.14) on the left-hand side, where $F$ and its derivative are evaluated at $R = R_0 - \rho$ also, the Bona-Massó equation becomes

$$\partial_n \left( (-F)^{-1/2} \partial_n \rho \right) = -\alpha^2 f(\alpha)(K(R_0) - \rho K'(R_0)) \tag{5.17}$$

to linear order in the perturbation $\rho$, where we have not yet evaluated the term $\alpha^2 f(\alpha)$. We note that we can evaluate $K(R_0) = K_0(R_0)$ using Eq. (4.28) once we evaluate $\alpha^2 f(\alpha)$. Remarkably, all spatial derivatives of $\rho$ other than those contained in the operators $\partial_n$ disappear in the limit $h_0' \to \infty$, resulting in an *ordinary* differential equation for $\rho$ at the puncture. In the next section we will see that the choice of $f(\alpha)$ determines whether Eq. (5.17) is of first or second order, thereby changing the qualitative behavior of the solutions.

## 5.3 Results

### 1 + log Slices

For almost all slicing conditions, the leading-order mean curvature term $K(R_0)$ on the right-hand side of Eq. (5.17) is nonzero. One such condition is $1 + \log$ slicing (4.3) with $k = 2$, for which Eq. (5.17) becomes

$$\partial_n\left((-F)^{-1/2}\partial_n\rho\right) = 2(-F)^{-1/2}\partial_n\rho(K(R_0) - \rho K'(R_0)) \tag{5.18}$$

upon using Eq. (5.14) for $\alpha$ on the right-hand side. We now observe that, to leading order in $\rho$, the term $\rho K'(R_0)$ on the right-hand side vanishes and with it the only appearance of $\rho$ itself (rather than its derivatives). To linear order in $\rho$, we may therefore replace the term $(-F)^{-1/2}\partial_n\rho$ with $\alpha$ to obtain a first-order equation for the lapse alone,

$$\partial_n\alpha = -2\alpha K(R_0). \tag{5.19}$$

This equation is identical to our starting point, Eq. (4.1), except that now, in the linear limit, we assume the mean curvature $K$ to take a positive and constant value. In this case we may integrate to obtain

$$\alpha(R) = Ce^{-2K(R_0)t}, \tag{5.20}$$

where $C$ is a constant of integration, demonstrating that to linear order we should expect the central lapse of $1 + \log$ slices to decay exponentially. As warned in Sec. 5.1, the predictions of Eq. (5.20) differ quantitatively from the numerical data in Fig. 5.1. During the time interval $10 \lesssim tM^{-1} \lesssim 15$, when Fig. 5.1 suggests an approximately exponential decay, the numerical data fall off more rapidly than predicted by Eq. (5.20). A rough fit to

the numerical data suggests a time constant $\tau$ that is smaller than $(2K(R_0))^{-1}$ by about a factor of two. However, rather than staying constant, the mean curvature $K$ changes rapidly through this dynamical period as it transitions from its initial value of zero to the equilibrium value $K_0(R_0) \approx 0.301$. This suggests nonlinear terms are still important during this time. At later times, numerical error becomes important; in particular, the lapse settles down to a small but nonzero value that depends on the numerical resolution, so that exponential decay can no longer be observed.

## Shock-Avoiding Slices

For shock-avoiding slices, the unperturbed puncture is located at $R_0 = 3M/2$ so that the mean curvature $K(R_0)$ on the right-hand side of Eq. (5.17) vanishes. Inserting the shock-avoiding condition (4.5) into Eq. (5.17), we now obtain

$$\partial_n\left((-F)^{-1/2}\partial_n\rho\right) = \kappa K'(R_0)\rho, \tag{5.21}$$

where we have already neglected a term quadratic in $\rho$ on the right-hand side. In contrast to $1 + \log$ slicing, the term proportional to $\rho$ now dominates the right-hand side, so we cannot rewrite this second-order equation as a first-order equation for $\alpha$. We instead expand to linear order in $\rho$ to yield the harmonic oscillator equation

$$\partial_n^2\rho = -\omega^2\rho, \tag{5.22}$$

where the angular frequency

$$\omega = -\sqrt{-F}\kappa K'(R_0). \tag{5.23}$$

In the uncharged case $\lambda = 0$, we have

$$\omega\bigg|_{\lambda=0} = \frac{8\kappa}{9M^2}. \tag{5.24}$$

Accordingly, for $\lambda = 0$ the central lapse $\alpha_c$ performs harmonic oscillation with period

$$P\bigg|_{\lambda=0} = \frac{3\pi M}{\sqrt{2\kappa}}. \tag{5.25}$$

Note that we have assumed $\kappa > 0$ in the above equations, in agreement with our original assumption in the shock-avoiding slicing condition (4.5).

As in Sec. 5.3, we attempt a quantitative comparison with the Schwarzschild numerical data with some caution. Measuring the period of oscillation observed in the shock-avoiding slices around $130 \lesssim tM^{-1} \lesssim 170$, we obtain $P_1 \approx 8M$ with $\kappa = 1$ and $P_{2/3} \approx 11M$ with $\kappa = 2/3$ (even though the latter, in particular, shows some variation). Evaluating the period (5.25), on the other hand, we predict $P_1 \approx 6.7M$ and $P_{2/3} \approx 8.2M$. While we again encounter quantitative disagreement, we see that our analysis does explain the origin of the observed harmonic oscillation and correctly predicts that the period increases with decreasing $\kappa$.

We suspect that nonlinear terms cause the damping of the oscillations at early times as seen in Fig. 5.1. Once the amplitude is small enough, however, the oscillations should be governed by Eq. (5.22), which does not contain a damping term. Accordingly, one would expect these oscillations to persist at a small amplitude, which is consistent with the numerical data.

## 5.4   Summary

In this chapter we explored the origins of a qualitative contrast observed in simulations of Schwarzschild black holes. The lapse at the black-hole puncture appears to decay

approximately exponentially for $1 + \log$ slices, whereas for shock-avoiding slices the central lapse appears to undergo rough harmonic oscillation; this behavior is evident in Fig. 5.1. We employ a dynamical height-function approach (see Ch. 3) to black-hole spacetimes whose line element takes the form (3.2) in order to represent time-dependent coordinate transitions. We then impose the Bona-Massó slicing condition (4.1) to construct trumpet slices and consider small perturbations in a background trumpet solution at the black-hole puncture. Describing these perturbations in terms of a small displacement $\rho$ in the radial coordinate of the puncture, the Bona-Massó equation becomes a second-order ODE (5.17) for $\rho$ in the normal derivative (5.13).

The primary difference between $1 + \log$ and shock-avoiding slices then arises from the behavior of the unperturbed mean curvature $K(R_0)$ evaluated at the puncture. For $1 + \log$ slicing, $K(R_0)$ takes a positive value, causing $\rho$ to drop out of the equation to linear order. This results in a first-order equation that governs exponential decay. For shock-avoiding slices, $K(R_0)$ vanishes, and the right-hand side of Eq. (5.17) becomes dominated by $\rho$ at linear order. The equation therefore remains a second-order ODE for $\rho$, resulting in harmonic oscillation. We observe that the period of oscillation varies inversely with the square root of the constant $\kappa$ in Eq. (4.5).

While a quantitative comparison of our analytical predictions with the numerical results of [57] shows some discrepancies as discussed in Sec. 5.1, we believe that these can be explained in terms of nonlinear effects, numerical error at the black-hole puncture, and our assumption that $\rho'$ remains finite, which may be restrictive. Despite these discrepancies, our work provides analytical insight into the dynamical behavior of the central lapse, points to the origin of qualitative differences between slicing conditions, and predicts the dependence of decay constants and oscillation periods on the slicing parameters.

# 6 Conclusion

In this thesis we examine the geometry of spatial hypersurfaces, or slices, of spacetimes of charged black holes. In particular, we study a set of coordinate gauge conditions known as the Bona-Massó slicing conditions, given by Eq. (4.1). These PDEs relate the lapse function $\alpha$, shift vector $\beta^i$, and mean curvature $K$ and are parametrized by the Bona-Massó function $f(\alpha)$ of the lapse. In Ch. 1 we motivate our analysis and introduce the above geometric quantities. In Ch. 2 we discuss two exact solutions to Einstein's equations, namely the Schwarzschild and Reissner-Nordström spacetimes, representing single, nonrotating, uncharged and charged black holes. In Ch. 3 we discuss the height-function approach used to carry out transformations of the time coordinate and obtain key results for both static and dynamical slices. In Ch. 4 we extend the analysis in [52] to static Reissner-Nordström spacetimes by introducing the black-hole charge-to-mass ratio $\lambda \equiv Q/M$. We compute properties of static $1 + \log$, analytical trumpet, shock-avoiding, and zero order shock-avoiding slices (see Sec. 4.1) of RN spacetimes and conclude that, in the extremal limit $\lambda \to 1$, all slices converge to a unique slice independently of the choice of Bona-Massó function. In Ch. 5 we study dynamical $1 + \log$ and shock-avoiding slices in an attempt to explain their qualitative behaviors observed in a recent numerical simulation [57]. We begin by recovering well-known gauge modes in the Minkowski limit $R \to \infty$ using a perturbation $\eta$ of the height function itself. We then employ a radial perturbation $\rho$ near the black-hole puncture to arrive at leading-order equations for the central lapse $\alpha_c$ that predict exponential decay and harmonic oscillation. These results

agree with the observed behaviors qualitatively despite some quantitative disagreement in the decay constants and periods of oscillation. Since the metric is written in terms of a function $F(R)$ that one may choose, the analysis in Ch. 5 applies to both Schwarzschild and RN spacetimes.

Astronomers rely on the predictions of numerical relativity to interpret gravitational-wave signals emitted by some of the most energetic processes in the Universe, such as black-hole and neutron-star collisions. To simulate such processes on a computer long enough to extract useful results, a numerical relativist needs to choose a suitable coordinate gauge, or slicing condition. We can better understand the most successful of these conditions by stepping back and taking slices of simple, analytically known spacetimes such as single, stationary black holes. This has been done numerous times for Schwarzschild spacetimes (e.g., [16]), but Reissner-Nordström spacetimes have received little attention in this context since the black-hole charge is usually assumed to be negligible. However, a number of authors [29–40] have recently assessed the role of the black-hole charge and simulated the interactions of charged black holes. This thesis adds to that work by providing insight into slicing conditions for RN spacetimes. Our results generalize those of [52] to charged black holes and resolve a mystery regarding the dynamical behavior of two useful slicing conditions.

# Acknowledgments

# References

[1] A. Einstein, The Field Equations of Gravitation, Sitzungsber. Preuss. Akad. Wiss. Berlin (Math. Phys.) **1915**, 844 (1915).

[2] S. M. Carroll, *Spacetime and Geometry: An Introduction to General Relativity* (Cambridge University Press, 2019).

[3] A. Einstein, Approximative Integration of the Field Equations of Gravitation, Sitzungsber. Preuss. Akad. Wiss. Berlin (Math. Phys.) **1916**, 688 (1916).

[4] B. P. Abbott, R. Abbott, T. D. Abbott, M. R. Abernathy, F. Acernese, K. Ackley, C. Adams, T. Adams, P. Addesso, R. X. Adhikari, V. B. Adya, C. Affeldt, M. Agathos, K. Agatsuma, N. Aggarwal, O. D. Aguiar, L. Aiello, A. Ain, P. Ajith, B. Allen, A. Allocca, P. A. Altin, S. B. Anderson, W. G. Anderson, K. Arai, M. A. Arain, et al. (LIGO Scientific Collaboration and Virgo Collaboration), Observation of Gravitational Waves from a Binary Black Hole Merger, Phys. Rev. Lett. **116**, 061102 (2016).

[5] M. C. Miller and N. Yunes, The new frontier of gravitational waves, Nature **568**, 469 (2019).

[6] B. P. Abbott, R. Abbott, T. D. Abbott, M. R. Abernathy, F. Acernese, K. Ackley, C. Adams, T. Adams, P. Addesso, R. X. Adhikari, V. B. Adya, C. Affeldt, M. Agathos, K. Agatsuma, N. Aggarwal, O. D. Aguiar, L. Aiello, A. Ain, P. Ajith, B. Allen, A. Allocca, P. A. Altin, S. B. Anderson, W. G. Anderson, K. Arai, M. C. Araya, et al. (LIGO Scientific and Virgo Collaborations), Tests of General Relativity with GW150914, Phys. Rev. Lett. **116**, 221101 (2016).

[7] M. Arca Sedda et al., The missing link in gravitational-wave astronomy: discoveries waiting in the decihertz range, Class. Quant. Grav. **37**, 215011 (2020).

[8] E. Barausse et al., Massive Black Hole Merger Rates: The Effect of Kiloparsec Separation Wandering and Supernova Feedback, Astrophys. J. **904**, 16 (2020).

[9] M. Maggiore et al., Science case for the Einstein telescope, J. Cosmol. Astropart. Phys. **2020**, 050 (2020).

[10] R. L. Arnowitt et al., The dynamics of general relativity, Gen. Rel. Grav. **40**, 1997 (2008).

[11] L. Smarr and J. W. York, Kinematical conditions in the construction of spacetime, Phys. Rev. D **17**, 2529 (1978).

[12] T. W. Baumgarte and S. L. Shapiro, *Numerical Relativity: Starting from Scratch* (Cambridge University Press, Feb. 2021).

[13] M. Shibata and T. Nakamura, Evolution of three-dimensional gravitational waves: Harmonic slicing case, Phys. Rev. D **52**, 5428 (1995).

[14] T. W. Baumgarte and S. L. Shapiro, On the numerical integration of Einstein's field equations, Phys. Rev. D **59**, 024007 (1998).

[15] M. D. Duez et al., Relativistic magnetohydrodynamics in dynamical spacetimes: Numerical methods and tests, Phys. Rev. D **72**, 024028 (2005).

[16] M. Hannam, S. Husa, D. Pollney, et al., Geometry and regularity of moving punctures, Phys. Rev. Lett. **99**, 241102 (2007).

[17] T. Yamamoto et al., Simulating coalescing compact binaries by a new code SACRA, Phys. Rev. D **78**, 064054 (2008).

[18] B. Bruegmann, Schwarzschild black hole as moving puncture in isotropic coordinates, Gen. Rel. Grav. **41**, 2131 (2009).

[19] J. B. Mertens et al., Integration of inhomogeneous cosmological spacetimes in the BSSN formalism, Phys. Rev. D **93**, 124059 (2016).

[20] T. W. Baumgarte and S. L. Shapiro, *Numerical Relativity: Solving Einstein's Equations on the Computer* (Cambridge University Press, 2010).

[21] B. Bruegmann, Binary black hole mergers in 3-d numerical relativity, Int. J. Mod. Phys. D **8**, 85 (1999).

[22] F. Pretorius, Evolution of binary black hole spacetimes, Phys. Rev. Lett. **95**, 121101 (2005).

[23] M. Campanelli et al., Accurate evolutions of orbiting black-hole binaries without excision, Phys. Rev. Lett. **96**, 111101 (2006).

[24] J. G. Baker et al., Gravitational wave extraction from an inspiraling configuration of merging black holes, Phys. Rev. Lett. **96**, 111102 (2006).

[25] F. Pretorius, Numerical relativity using a generalized harmonic decomposition, Class. Quant. Grav. **22**, 425 (2005).

[26] C. Bona et al., New Formalism for Numerical Relativity, Phys. Rev. Lett. **75**, 600 (1995).

[27] M. Hannam, S. Husa, B. Bruegmann, et al., Where do moving punctures go?, J. Phys. Conf. Ser. **66**, edited by P. Apostolopoulos et al., 012047 (2007).

[28] M. Hannam, S. Husa, F. Ohme, et al., Wormholes and trumpets: The Schwarzschild spacetime for the moving-puncture generation, Phys. Rev. D **78**, 064020 (2008).

[29] M. Alcubierre et al., Einstein-Maxwell system in $3 + 1$ form and initial data for multiple charged black holes, Phys. Rev. D **80**, 104022 (2009).

[30] M. Zilhão et al., Collisions of charged black holes, Phys. Rev. D **85**, 124062 (2012).

[31] M. Zilhão et al., Collisions of oppositely charged black holes, Phys. Rev. D **89**, 044008 (2014).

[32] M. Zilhão et al., Head-On Collisions of Charged Black Holes from Rest, Springer Proc. Math. Stat. **60**, edited by A. García-Parrado et al., 451 (2014).

[33] M. Zilhão et al., Dynamics of Charged Black Holes, in *Proceedings of the Thirteenth Marcel Grossmann Meeting on Recent Developments in Theoretical and Experimental General Relativity, Astrophysics, and Relativistic Field Theories* (World Scientific, Singapore, 2015), pp. 983–985.

[34] P. Jai-akson et al., Black hole merger estimates in Einstein-Maxwell and Einstein-Maxwell-dilaton gravity, Phys. Rev. D **96**, 044031 (2017).

[35] P. K. Gupta et al., Bounding dark charges on binary black holes using gravitational waves, Phys. Rev. D **104**, 063041 (2021).

[36] G. Bozzola and V. Paschalidis, General Relativistic Simulations of the Quasicircular Inspiral and Merger of Charged Black Holes: GW150914 and Fundamental Physics Implications, Phys. Rev. Lett. **126**, 041103 (2021).

[37] G. Bozzola and V. Paschalidis, Numerical-relativity simulations of the quasicircular inspiral and merger of nonspinning, charged black holes: Methods and comparison with approximate approaches, Phys. Rev. D **104**, 044004 (2021).

[38] G. Bozzola, Does Charge Matter in High-Energy Collisions of Black Holes?, Phys. Rev. Lett. **128**, 071101 (2022).

[39] S. Mukherjee et al., Conformally curved initial data for charged, spinning black hole binaries on arbitrary orbits, Feb. 2022, arXiv:2202.12133 [gr-qc].

[40] R. Luna et al., Kicks in charged black hole binaries, Phys. Rev. D **106**, 084017 (2022).

[41] G. W. Gibbons, Vacuum Polarization and the Spontaneous Loss of Charge by Black Holes, Commun. Math. Phys. **44**, 245 (1975).

[42] J. W. Moffat, Scalar–tensor–vector gravity theory, J. Cosmol. Astropart. Phys. **2006**, 004 (2006).

[43] K. Schwarzschild, On the gravitational field of a mass point according to Einstein's theory, Sitzungsber. Preuss. Akad. Wiss. Berlin (Math. Phys.), 189 (1916).

[44] W. Israel, Event Horizons in Static Vacuum Space-Times, Phys. Rev. **164**, 1776 (1967).

[45] W. Israel, Event horizons in static electrovac space-times, Commun. Math. Phys. **8**, 245 (1968).

[46] B. Carter, Axisymmetric Black Hole Has Only Two Degrees of Freedom, Phys. Rev. Lett. **26**, 331 (1971).

[47] H. Reissner, Über die Eigengravitation des elektrischen Feldes nach der Einsteinschen Theorie, Annalen der Physik **355**, 106 (1916).

[48] A. P. Lightman et al., *Problem Book in Relativity and Gravitation* (Princeton University Press, 1975).

[49] S. E. Li, T. W. Baumgarte, K. A. Dennison, and H. P. de Oliveira, Bona-Massó slices of Reissner-Nordström spacetimes, Phys. Rev. D **106**, 104059 (2022).

[50] P. Anninos et al., Three-dimensional numerical relativity: The evolution of black holes, Phys. Rev. D **52**, 2059 (1995).

[51] T. W. Baumgarte and S. G. Naculich, Analytical representation of a black hole puncture solution, Phys. Rev. D **75**, 067502 (2007).

[52] T. W. Baumgarte and H. P. de Oliveira, Bona-Masso slicing conditions and the lapse close to black-hole punctures, Phys. Rev. D **105**, 064045 (2022).

[53] K. A. Dennison and T. W. Baumgarte, A Simple Family of Analytical Trumpet Slices of the Schwarzschild Spacetime, Class. Quant. Grav. **31**, 117001 (2014).

[54] M. Alcubierre, Appearance of coordinate shocks in hyperbolic formalisms of general relativity, Phys. Rev. D **55**, 5981 (1997).

[55] M. Alcubierre, Hyperbolic slicings of space-time: Singularity avoidance and gauge shocks, Class. Quant. Grav. **20**, 607 (2003).

[56] E. Jiménez-Vázquez and M. Alcubierre, Critical gravitational collapse of a nonminimally coupled scalar field, Phys. Rev. D **105**, 064071 (2022).

[57] T. W. Baumgarte and D. Hilditch, Shock-avoiding slicing conditions: Tests and calibrations, Phys. Rev. D **106**, 044014 (2022).

[58] J. R. van Meter et al., How to move a black hole without excision: Gauge conditions for the numerical evolution of a moving puncture, Phys. Rev. D **73**, 124011 (2006).

[59] K. A. Dennison, T. W. Baumgarte, and P. J. Montero, Trumpet Slices in Kerr Spacetimes, Phys. Rev. Lett. **113**, 261101 (2014).

[60] J. Healy et al., High energy collisions of black holes numerically revisited, Phys. Rev. D **94**, 104020 (2016).

[61] I. Ruchlin et al., Puncture initial data for black-hole binaries with high spins and high boosts, Phys. Rev. D **95**, 024033 (2017).

[62] S. E. Li, T. W. Baumgarte, K. A. Dennison, and H. P. de Oliveira, Dynamical perturbations of black-hole punctures: Effects of slicing conditions, Phys. Rev. D **107**, 064003 (2023).

[63] H. P. de Oliveira, Multidomain spectral code for punctures without excision: The spherical case, Phys. Rev. D **106**, 084030 (2022).